FROM NUMBERS TO INSIGHTS: COMPUTATIONAL STUDIES OF COMPLEX ORGANIC SYSTEMS

by

SHARATH CHANDRA MALLOJJALA

(Under the Direction of Steven Wheeler)

ABSTRACT

Computational chemistry has been widely used to investigate chemical systems and to infer properties relating their structure and reactivity. The advent of modern density functional theory (DFT) methods has made computations on complex organic systems with 50-150 atoms feasible, and accurate relative free energies and enthalpies of transition states can be computed using DFT methods for mechanistic investigations of organic reactions. I have used modern computational tools to investigate aza-thia cryptands with important host-guest applications, the ground state structure of [18]annulene, the observed stereo-reversal in an epoxide desymmetrization reaction catalyzed by a chiral metal phosphate compared to a chiral phosphoric acid, and the role hexafluoroisopropanol, a widely used polar solvent for C-H functionalization reactions, in a palladium catalyzed C-H alkylation reaction. I have used DFT methods and modern analysis techniques to study these complex organic systems and turn the numbers provided by computations into chemically meaningful insights.

INDEX WORDS: computational chemistry, density functional theory, macrocyclic systems. organocatalysis, metal catalysis, structure elucidation, mechanistic investigation

FROM NUMBERS TO INSIGHTS: COMPUTATIONAL STUDIES OF COMPLEX ORGANIC SYSTEMS

by

SHARATH CHANDRA MALLOJJALA

B.S.M.S, Indian Institute of Science Education and Research-Pune, 2015

A Dissertation Submitted to the Graduate Faculty of The University of Georgia in Partial Fulfillment of the Requirements for the Degree

DOCTOR OF PHILOSOPHY

ATHENS, GEORGIA

2019

FROM NUMBERS TO INSIGHTS: COMPUTATIONAL STUDIES OF COMPLEX ORGANIC SYSTEMS

by

SHARATH CHANDRA MALLOJJALA

Major Professor:	Steven E. Wheeler
Committee:	Henry F. Schaefer
	Eric M. Ferreira

Electronic Version Approved:

Ron Walcott
Interim Dean of the Graduate School
The University of Georgia
December 2019

DEDICATION

To Dr. Harinath Chakrapani, my undergraduate advisor, for helping me whenever I was lost and in need of guidance.

ACKNOWLEDGEMENTS

I would like to thank my doctoral advisor, Dr Steven Wheeler for not only accepting me as a graduate student but also for all the mentorship he provided and for being patient, helpful, and kind to me in all the circumstances. He helped ease my transition to Texas A&M University and later to University of Georgia. I would like to thank my committee members Dr Schaefer and Dr Ferreira for providing helpful advice and being very accommodating in managing the deadlines. I would also like to thank Dr Allinger, Dr Walker and Dr Taschner for being valuable collaborators and providing useful inputs during project discussions.

I like to thank past Wheeler group members Trevor and Andrea for providing valuable insights during group meetings. It was a pleasure to collaborate with Rajat, who was also a very good mentor figure and helped me through these five years. I also thank Yanfei, Stephen, Drew, Bryan, Victoria, Aarya, Tony, and Laura for being a pleasure to work with and for all the time we spent playing boardgames and sports. I also like to acknowledge Laura’s help in proof-reading my thesis. I also thank Kathryn and Sybil for all the help they provided throughout my time at the CCQC and the rest of CCQC for making it a wonderful place to work at. I would also like to thank my friends Nishad, Nisarg, Madhur, and Himanshu for being understanding whenever I had to rant about stuff in my life.

Finally, I would like to thank my family who have been very supportive of all my decisions throughout my life. I wouldn’t have managed these past years without the

support of Mom (Savithri) & Dad (Bhavanandam), and my brother (Srikanth). I also take this opportunity to thank my uncles (Srinivas and Shravan), my aunts (Rajeshwari and Lalitha) and my grandmother (Vasantha) for teaching me various things growing up and taking care of me.

TABLE OF CONTENTS

Page

APPENDICES

CHAPTER 1

INTRODUCTION, BACKGROUND MATERIAL AND LITERATURE REVIEW

1.1 Introduction

Historically, computational chemistry has been extensively used[1-2] as an interpretative tool to decipher the structure,[3-6] spectra,[7-10] and reactivity[1, 11-13] of complex chemical systems. Early computational efforts to understand complex organic systems utilized molecular mechanics (MM), a classical mechanics-based approach to model molecular structures. Despite providing reliable thermochemical data, they are restricted by the availability of parameters for specific atom types.[14-16] Moreover, MM methods are unable to provide insights into the electronic properties of the molecules being studied. This can be overcome by solving the electronic Schrödinger equation using *ab initio* methods to obtain the many electron wavefunction of the system. Solving the electronic Schrödinger equation exactly for any but the smallest of molecules is computationally prohibitive. This computational complexity problem can be alleviated by using density functional theory (DFT) methods. DFT methods provide a massive reduction in computational cost at a minimal loss in accuracy compared to correlated *ab initio* methods. This, coupled with continuing advances in semiconductor technology, development of new hybrid functionals, and empirical dispersion corrections[17] have allowed for routine applications of sophisticated computer simulations for large molecules.[15, 18-30] Furthermore, the development and implementation of numerous analysis techniques such as distortion-interaction analysis,[31-35] symmetry-adapted perturbation theory (SAPT),[36-40] NCI plots,[41] among others have transformed molecular modelling from an interpretative tool to a predictive tool.

1.2 Analysis techniques

The many methods of electronic structure theory provide structures and energetics for key intermediates and transition state structures. However, unraveling the origins of the energy differences that underpin chemical phenomena (selectivity, reactivity, *etc.*) require careful analyses of these structures and their underlying electronic structure. The key analysis tools utilized throughout this dissertation are described briefly below, and include distortion-interaction analysis[31-35] and electrostatic potential maps and slices.[42-45]

1.2.1 Distortion-Interaction analysis

Distortion-interaction analysis or the activation-strain model[31-35] is an energy decomposition scheme to understand the origin of reactivity and selectivity of molecules and reactions. Morokuma[34] and Ziegler and Rouk[35] first applied this analysis quantitatively to study stable molecules. Houk and Bickelhaupt[31-33] later extended this method independently to study equilibrium structures, non-stationary points, and transition state (TS) structures. In the distortion-interaction/activation-strain model, the energy along a potential energy surface can be decomposed into two components, the strain (or distortion) and the interaction energy between these distorted fragments (equation 1) along the reaction coordinate (ζ):

$$\Delta E(\zeta) = \Delta E_{strain}(\zeta) + \Delta E_{interaction}(\zeta)$$

This approach can be illustrated using transition states for a simple 1,3-dipolar cycloaddition reaction (see Scheme 1) from Ess and Houk.[32] The distortion component (or the activation-strain energy) of the barrier height is the energy required to deform the isolated reactants (*viz.*, nitrous oxide and ethylene) into their TS geometries without allowing for the interaction (See Figure 1). Distortion raises the barrier height as the nitrous oxide distorts into a bent geometry and the ethylene loses its planarity. The interaction component is the stabilization arising from bringing these two distorted fragments together, lowering the reaction barrier.

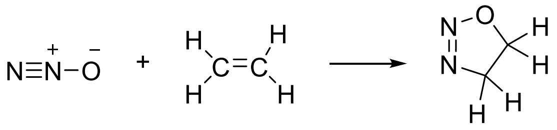

Scheme 1 Huisgen's 1,3-dipolar addition of nitrous oxide with ethylene.

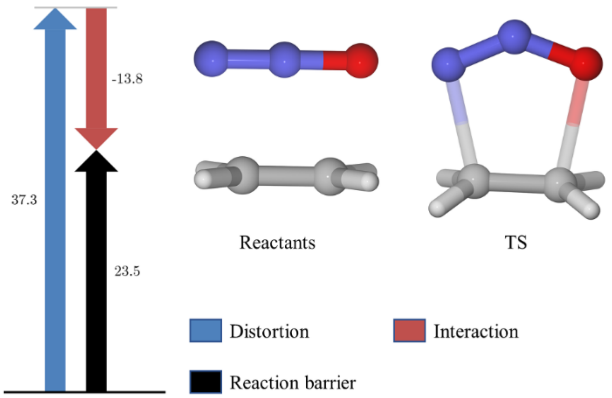

Figure 1 A distortion-interaction plot for 1,3-dipolar cycloaddition reaction reported by Ess and Houk[32] (in kcal/mol).

While this analysis is most commonly applied to transition state geometries, it can be applied to any point on a potential energy surface, most commonly along computed intrinsic reaction coordinates (IRC). Generally, the distortion component is positive and raises the reaction barrier while interaction component is negative and lowers the reaction barrier. However, in the case of some cycloaddition reactions, the interaction energy can be positive and repulsive in the early stages of the reaction. The interplay between distortion/activation-strain and interaction energy determines the reaction barrier, and the separation of these contributions can often help pinpoint differences in barrier heights for stereoselective reactions, *etc*.

1.2.1 Electrostatic potential slices

Non-covalent interactions, including hydrogen bonding interactions and chalcogen bonding interactions, have been shown to play key roles in enzyme catalysis,[46-48] drug binding, organocatalysis,[44-45, 49-53] and transition metal catalysis.[54-55] These interactions are predominantly electrostatic in nature. Wheeler, *et al*.[19, 29, 43-45, 49-51] Cheong, *et al*.[28] and Jacobsen, *et al*.,[56-57] among others,[26, 52-53] have demonstrated the importance of understanding and modulating these interactions in catalytic systems. A rigorous quantitative approach for understanding these interactions involves the use of various energy decomposition schemes such as the Kituara-Morokuma energy decomposition scheme[58] or symmetry-adapted perturbation theory (SAPT).[36-39]

One less-utilized but no less powerful approach to quantifying non-covalent interactions in stereocontrolling TS structures uses a combination of atomic charges derived from natural population analysis (NPA)[59-60] and electrostatic potential slices (ESP).[42-45] For example, Seguin and Wheeler[45] used ESP slices along with NPA charges to explain the *endo* selectivity observed in a chiral anion directed Diels-Alder reaction (see Scheme 2). In particular, the ESP due to the catalyst on the reactants along a plane containing key atoms involved in CH···O interactions revealed favorable interactions in the case of the preferred diastereomer (see Figure 2).

This approach is quite general, and ESP slices along various planes can give insights into different stabilizing and destabilizing interactions responsible for the observed selectivity. Generally, the ESP due to the larger fragment (the chiral anion in Figure 2) is computed in the vicinity of the smaller fragment (the diene and dienophile together in Figure 2).

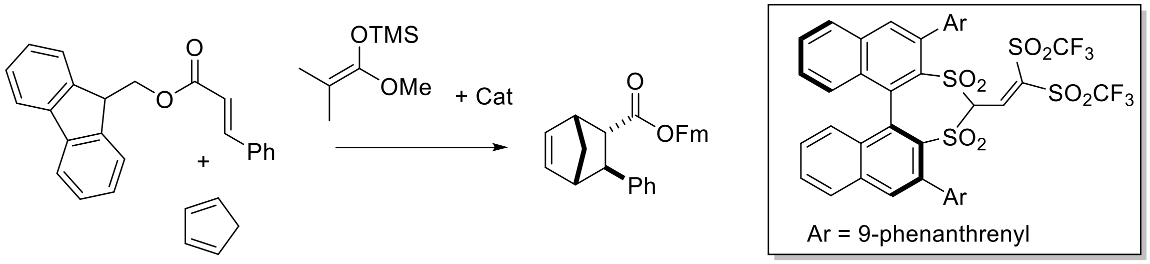

Scheme 2 Chiral anion directed Diels-Alder reaction studied by Seguin and Wheeler.[45]

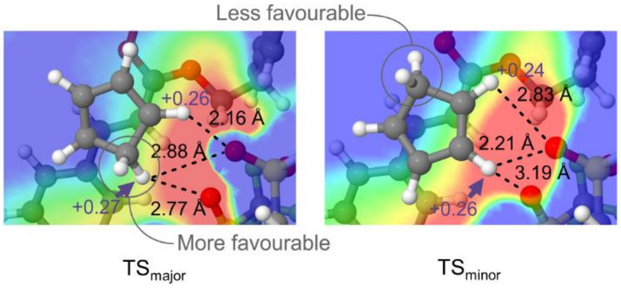

Figure 2 Electrostatic slice along the plane containing a key CH…O interaction reported by Seguin and Wheeler.[45] Red/blue regions indicate stabilizing/destabilizing interactions for positively charged species.

1.3 Motivation for the computational studies

Armed with these techniques, I have studied numerous complex chemical systems. First, I studied a series of cryptands using molecular mechanics and DFT techniques to understand their pore size tunability and their ability to bind copper(I) and Cu(II) ions. Secondly, I applied DFT methods in conjunction with more robust *ab initio* methods to study the ground state structure and understand the mechanism behind coalescence of the NMR chemical shifts at elevated temperatures observed in [18]annulene. Thirdly, I studied an organocatalyzed thiolysis of epoxides to understand the role played by alkali and alkaline earth metal salts of chiral phosphoric acid (CPA). Finally, I applied DFT methods to investigate the role of hexafluoroisopropanol (HFIP) and a silver salt in a palladium catalyzed *meta-selective* C-H activation reaction.

1.3.1 Motivation for studying cryptands

Metalloenzymes, which are enzymes with metal cofactors, make up a third of known enzymes. They are involved in numerous processes including electron-transfer reactions[61-62] and the storage and transportation of proteins.[63] Copper containing metalloenzymes like plastocyanin and azurin have garnered significant interest as potential therapeutic agents for various diseases. Studying how Cu(I) and Cu(II) are bound to both hard and soft nucleophiles present in biological systems will further our understanding of these metalloenzymes. To this end, there is a necessity for computationally tractable model systems. Cryptands are macrobicyclic polydentate systems first synthesized by Jean-Marie Lehn.[64] They have been used extensively for host-guest applications such as ion trapping, metal extraction, molecular recognition, and as molecular motors. Oxygen containing cryptands like Cryptand [2.2.2], have been studied extensively. However, aza-thia cryptands haven’t been studied synthetically or computationally. These aza-thia cryptands can serve as model systems to study the copper binding affinity in blue copper proteins. Moreover, studying the pore size tunability of these macrocycles opens the door for designing new cryptands with enhanced ion-binding abilities. In Chapter 2, I study a series of cryptands to develop a general understanding of their structure, conformations, and Cu-binding abilities.

1.3.2 Motivation for studying [18]annulene

There has been a long-standing interest in the study of annulenes aimed at understanding the system size at which a fully delocalized π system gives way to a poly-ene like character. Moreover, studying annulenes can further our fundamental understanding of aromaticity. Annulenes may be broadly divided into two classes, *viz.*, [4n]annulenes and [4n+2]annulenes, based on the π electron count. Schleyer and coworkers[65] investigated a series of [4n+2]annulenes and identified [18]annulene to be the tipping point where delocalized π systems give way to poly-ene like nature. A later study by Schleyer and coworkers[66] on the structure of [18]annulene further solidified this claim by demonstrating the ground state structure of [18]annulene to be a bond alternating poly-ene. However, further studies[67-68] on the geometry of [18]annulene reported the ground state to be bond-equal. Moreover, there has been a long-standing discrepancy[69-70] between the experimental enthalpy of formation values for this system. Finally, Oth[71] observed that the two distinct proton chemical shifts of [18]annulene coalesce into a single peak at elevated temperatures and proposed a formal pathway for this process. However, this pathway has not been studied computationally, and other possible pathways for this observed coalescence have not been explored. In Chapter 3, I study these three problems using DFT and *ab initio* methods.

1.3.3 Motivation for studying organocatalyzed epoxide thiolysis

Axially chiral motifs based on the binaphthol (BINOL) framework have been used extensively as organocatalysts for stereoselective reactions.[19, 72-73] One such class of organocatalysts are chiral phosphoric acids (CPA) and their derivatives, which have seen a rapid rise in their use in organic synthesis. However, these catalysts were found to be readily neutralized by alkali and alkaline earth metals present in the silica gel used for purifying these compounds. Rueping,[74] Ding,[75] and Ishihara[76] independently reported the importance of acidic purification of these CPAs. Moreover, some of these alkali and alkaline earth metal salts of chiral phosphates (CMP) demonstrated a stereo reversal to that of CPAs. However, the origin of this stereo reversal was not understood. In Chapter 4, I report computational studies on a chiral lithium BINOL phosphate catalyzed epoxide thiolysis reported by Antilla and coworkers[77] to understand the role played by alkali metals in stereo reversal.

1.3.3 Motivation for studying palladium catalyzed alkylation

Directing group assisted[78] palladium catalyzed C-H functionalization reactions are used extensively to do site-selective substitutions on arenes. Typically, these reactions use silver salts as co-catalysts to enhance the rate of the reaction. Houk and coworkers[79] demonstrated that palladium silver complexes and palladium dimer complexes also catalyze these reactions and are often the most favorable pathways. Moreover, recent experimental studies by Maiti and coworkers[55, 80-81] identified hexafluoroisopropanol (HFIP), a commonly used[55, 81-82] solvent for numerous C-H functionalization reactions, to be vital for reactivity. There are no reports of computational studies on these reactions which address both the active catalyst responsible for the selectivity and the role of HFIP. In Chapter 5, I report computational studies on a *meta-selective* C-H alkylation reaction catalyzed by palladium acetate in the presence of a silver salt to understand the role played by HFIP and to identify the active catalysts.

CHAPTER 2

COMPUTATIONAL STUDIES OF AZA-THIA CRYPTANDS[a]

---

[a] Portions adapted with permission from T. L. Walker, I. S. Taschner, M. Sharath Chandra, M. J. Taschner, J. T. Engle, B. R. Schrage, C. J. Ziegler, X. Gao, and S. E. Wheeler, *J. Org. Chem.* **83**, 10025 (2018).

Abstract

We report computational studies on macrobicyclic aza-thia lactams and aza-thia cryptands to elucidate their structures, investigate their pore size tunability, and quantify their ability to bind Cu(I) and Cu(II) ions. Building on the 14 membered N_2S_2 template of Weisman and Wong, we systematically investigated three bicyclic lactams with bridgehead lengths of nine, eight, and seven carbons and their respective reduced forms using modern DFT methods. The lowest-lying geometries compared favorably to the X-ray crystallographic structures, thereby validating the computational methods employed. Furthermore, we investigated a tetra thia bicyclic lactam and cryptand modelled after the nine carbon bicyclic lactams and their ability to chelate Cu(I) and Cu(II) ions. Computed EPR spectra for the lowest-lying Cu(II) bound tetra thia bicyclic lactam and cryptand was in excellent agreement with the experimental EPR spectra, thereby establishing the coordination observed in the solution phase. Copper ions were found to exhibit six coordination with the sixth ligand at a larger than usual coordination distance, as observed in the metalloenzymes plastocyanin and azurin.

Introduction

The field of supramolecular chemistry has developed leaps and bounds since Pedersen,[83-84] Lehn,[64, 85] and Cram[86-88] discovered crown ethers and cryptands. These systems have been widely studied and used in host-guest applications including sensing,[86, 88] molecular recognition,[89-91] molecular motors, metal extraction, and self-organization in artificial molecular machines.[92-95] Of these two classes of host-guest systems, macrobicyclic polydentate systems (cryptands) have demonstrated markedly better selectivity and higher association constants compared to crown ethers, making them a suitable candidate for exploring the design space of these systems. Recent studies[96-97] have further demonstrated the power of cryptands as sensors for oncological studies and biomedical imaging compared to their crown ether equivalents. Growing interest in using copper containing radiotracers such as Cu(II)-diacetyl-bis(N^4-methylthiosemicarbazone) for detecting markers for cancerous cells such as hypoxic tissues has resulted in a need for designing better chelating agents for copper. Weisman and Wong[98] have focused their efforts on developing bicyclic polyamines (see Figure 3) capable of selectively chelating copper ions.

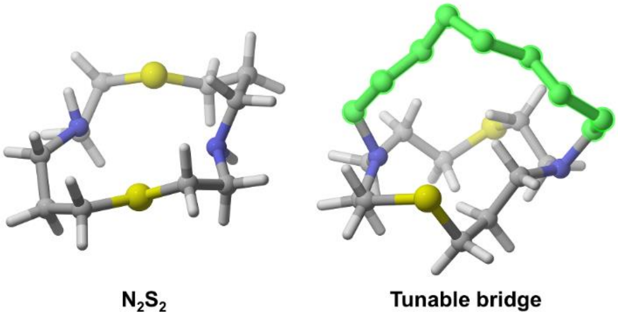

Figure 3 On the left is Weisman's N_2S_2 pore[98] and on the right is a model cryptand with the N_2S_2 core.

They reported[98] novel 14 membered cross-bridged cyclams with an N_2S_2 pore capable of acting as a chelating agent for radiolabeled copper for positron emission tomography (PET) imaging. Furthermore, their design was engineered to constrain the directionality of the lone pairs to afford stable metal ligates. However, little is known about the redox stability of Cu(I) and Cu(II) complexes of these systems.

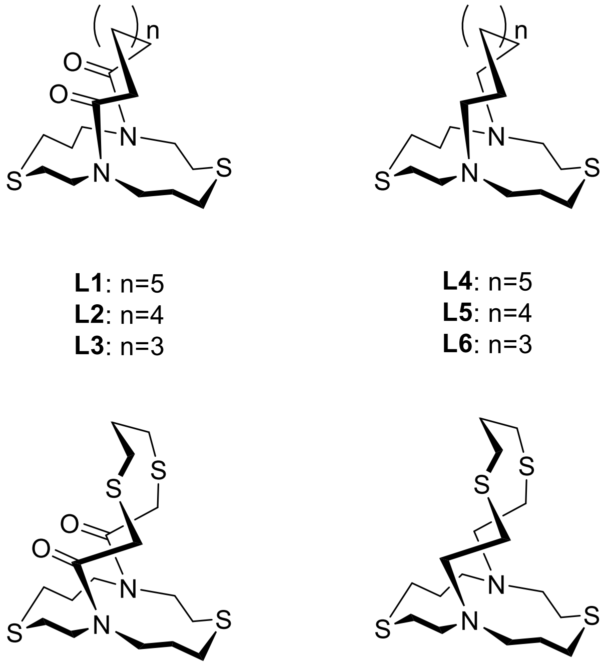

L1: n=5
L2: n=4
L3: n=3

L4: n=5
L5: n=4
L6: n=3

L7

L8

Scheme 3 Macrobicyclic lactams and cryptands investigated in this report.

Studying the chelating abilities of thioethers and thia-aza ligands can improve our understanding of blue copper proteins and copper containing metalloenzymes[61] such plastocyanin and azurin, which have sulfur containing ligands like cysteine that chelate the copper ions. Furthermore, these metalloproteins have garnered significant interest as potential therapeutic agents for various diseases. Unlike the chelating abilities of cryptands containing oxygen atoms (such as cryptand [2.2.2]), which have been extensively studied, there is a gap in our understanding of cryptands that contain softer atoms like sulfur. To understand these systems better, and building on Pedersen's work,[84] Busch,[99-100] Ochrymowycz,[101-104] and Rorabacher[102, 105-106] synthesized a series of macrobicyclic thioether and thia-aza ligands. Lippard and coworkers[107] synthesized a 14 member thia-aza ligand with an N_2S_2 pore and demonstrated its ability to bind and detect copper ions and nitroxyl species. The locations of the nitrogen atoms along with its ring size makes this scaffold a suitable candidate to incorporate a bridgehead to expand the design space for novel cryptands and to investigate the effects of incorporating a bridgehead on the pore size tunability of these systems. By varying the size and chemical composition of the bridgehead, insights into the tunability of binding strength and chelation ability of these new cryptands with Cu(I) and Cu(II) can be obtained, thereby furthering our understanding of blue copper proteins and other copper containing metalloenzymes.[61] Herein, we report computational studies of novel dithia-aza and tetrathia-aza cryptands using modern DFT methods. We also report computational studies of Cu(I) and Cu(II) complexes of tetrathia-aza cryptands to elucidate the structure and nature of coordination.

Results and Discussion

Building on the N_2S_2 pore of Weisman and Wong,[98] we first chose to explore the effects of incorporating a bridgehead on the pore size of these cryptands. For this, we chose to study lactams of N_2S_2 with bridge lengths of nine, eight, and second carbons

(L1-L3 in Scheme 3) and their corresponding amine cryptands (L4-L6 in Scheme 3). An exhaustive conformational search was performed for each of the lactams and cryptands. The global minimum energy conformations of L1-L6 are shown in Figure 4. Geometric parameters from the computed solution phase geometry (in chloroform) for L1 are in excellent agreement with the X-ray crystallography data provided by our experimental collaborators (see Table 1).

Table 1 Experimental (denoted with *) and computed geometric parameters for the lowest-lying lactams and cryptands with bridge length 9, 8, and 7 carbons.

Parameter	L1*	L1	L2	L3	L4	L5	L6
N···N	4.88	4.96	5.78	5.50	5.20	4.59	5.03
S···S	5.84	5.57	4.44	4.71	5.67	6.40	5.58
(∑CNC)	354, 359	358, 360	357, 357	358, 357	331, 332	341, 333	334, 332

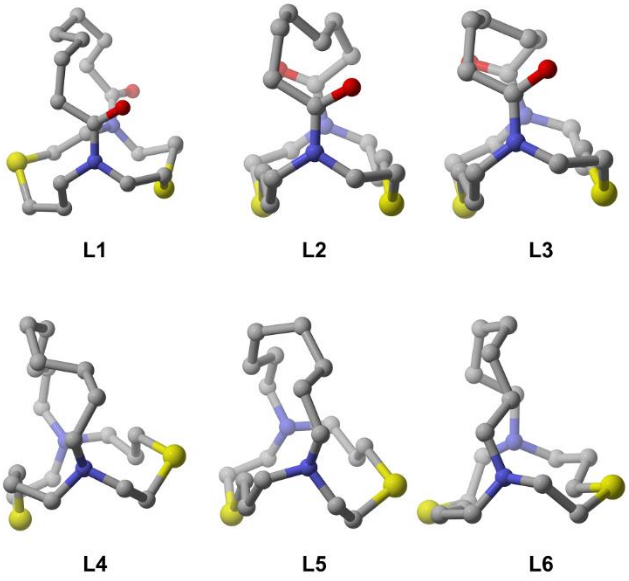

Figure 4 Computed lowest-lying geometries for lactams and amine cryptands with bridge lengths of 9, 8, and 7 carbons.

All the lactams (L1-L3) were predicted to exhibit two key low-lying rotameric forms (the rotamer of L1 is labeled LR1, etc.; see Figure 5). These rotamers differ in the orientation of the carbonyl groups: either both the carbonyl groups oriented parallel to each other or both the carbonyl groups oriented anti-parallel to each other. Strangely, for the largest lactam (L1) the global minimum energy rotamer features anti-parallel alignment of the carbonyl groups while for L2 and L3 the rotamer with parallel alignment of the carbonyl groups is favored. The smaller pore size in L2 and L3, in comparison to L1, was postulated as a one reason for this observation.

Transition states for the interconversion between these rotamers were located, and it was found that this conformational barrier decreases with decreasing bridge length (see Figure 5). The low-lying rotamers of L2 and L3 are expected to rapidly interconvert at room temperature, with barriers of ~20 kcal/mol. L3 and its rotamer (LR3) are similar in energy, so both rotamers are expected to be present at significant concentrations. L1 and its rotamer of L1 (LR1) are essentially isoenergetic. However, unlike L2 and L3 the barrier for interconversion is relatively high, suggesting that this system will be conformationally stable at room temperature.

The amine cryptands (L4-L6) were predicted to exhibit three topologies based on the lone pair orientation on the two nitrogen atoms: *in/in*, *in/out*, and *out/in*. Of these three topomers, the lowest-lying solution phase geometries were found to prefer an *in/in* topology. The incorporation of a bridging ligand was found to significantly alter the structure and conformation of the N_2S_2 pore. Moreover, lactams were found to have nearly planar nitrogen atoms owing to the delocalization of the nitrogen lone pairs into the C-O bonds. However, functionally, both cryptands and lactams are very similar to the 14 membered parent N_2S_2 pore.

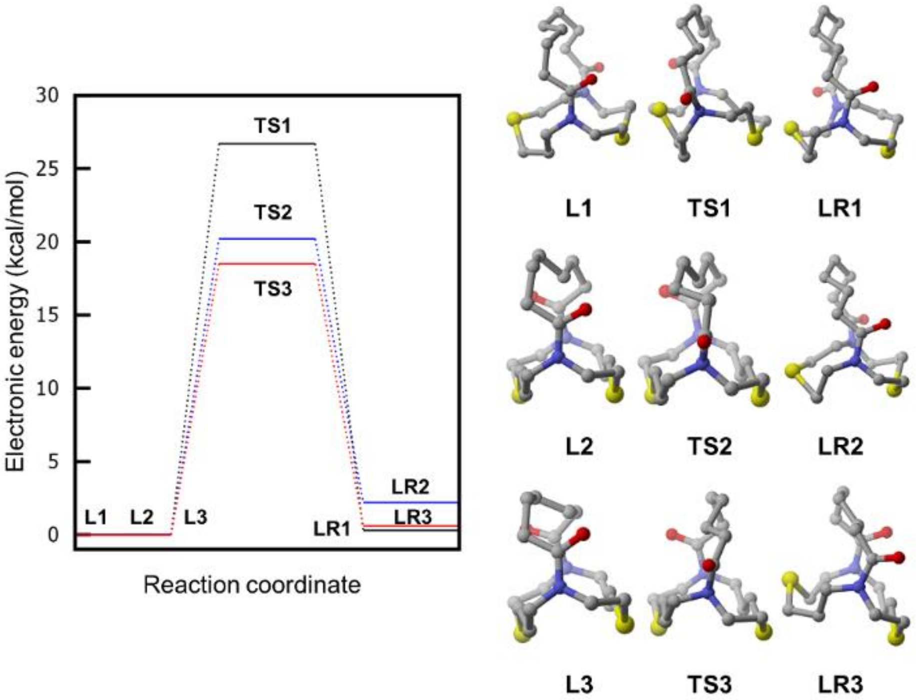

Figure 5 Computed barrier for rotamer interconversion of lactams with bridge lengths of 9, 8, and 7 carbons.

Owing to this, we chose to modify the bridge by replacing two of the carbons with sulfur to increase the chelation ability of these cryptands. Furthermore, upon examining the geometrical parameters for lactams and amine cryptands (Table 1), we identified L1 and L4 as suitable templates for further functionalization due to their large pore sizes (L7 and L8 in Scheme 3).

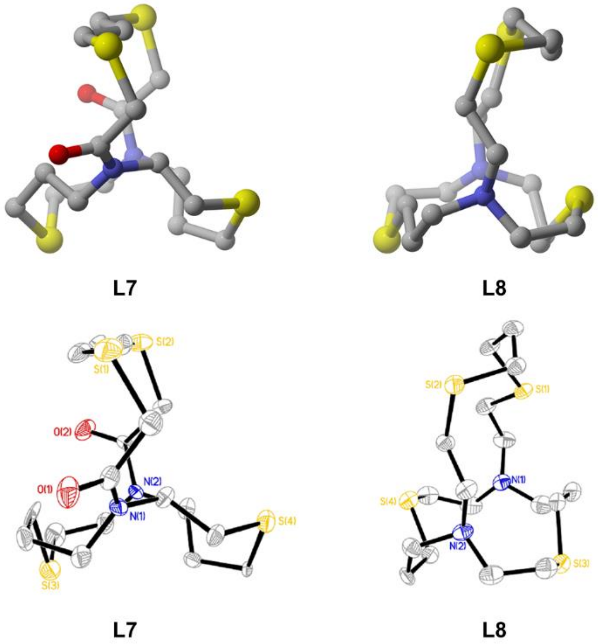

Figure 6 Computed lowest-lying conformers (top) for aza-thia lactam (L7) and aza-thia cryptand (L8) with their respective X-ray crystal structures (bottom). (Figure adapted from J. Org. Chem. 2018, 83, 17, 10025-10036.)

Computed geometrical parameters for the lowest-lying conformers of thia-aza cryptands L7 and L8 were found to be in excellent agreement with the X-ray crystallography data (see Table 2 and Figure 6).[108] L7 was found to exhibit two rotameric states based on the orientation of the carbonyl groups. Similar to L1, the lowest-lying rotamer was found to prefer parallel orientation of the carbonyl groups. However, the computed barrier for the rotamer interconversion in L7 was found to be lower than that of L1 by 2 kcal/mol (Figure 18, Appendix A). Furthermore, L8 was found to exhibit similar structural properties to L4, with the lowest-lying conformer opting *in/in* topology. A barrier of 10 kcal/mol was computed for the interconversion between the topomers

(Figure 19, Appendix A). Fragmentation analysis revealed lactam L7 to have a more strained N_2S_2 pore than the amine cryptand L8.

Table 2 Experimental (denoted by *) and computed geometric parameters for aza-thia lactam and aza-thia cryptand.[108]

Parameter	L7*	L7	L8*	L8
N···N	4.78	4.88	4.7	4.80
S···S	5.80	5.78	5.2	5.59
(∑CNC)	354, 359	358, 360	337, 331	337, 334

Finally, we chose to investigate Cu(I) and Cu(II) complexes of L7 and L8 to understand the experimentally observed preference of these cryptands for selectively stabilizing Cu(I). A thorough conformational search was performed to identify the lowest-lying Cu(I) and Cu(II) complexes of L7 and L8, which are depicted in Figure 7. Upon identifying the lowest-lying Cu(II) complexes for L8, electron paramagnetic resonance (EPR) spectra were computed for all of the conformers within 1 kcal/mol of the global minimum energy conformer. The computed EPR spectra were found to be in excellent agreement with the experimental EPR spectrum (see Table 3) thereby establishing the presence of these computed geometries in solution.

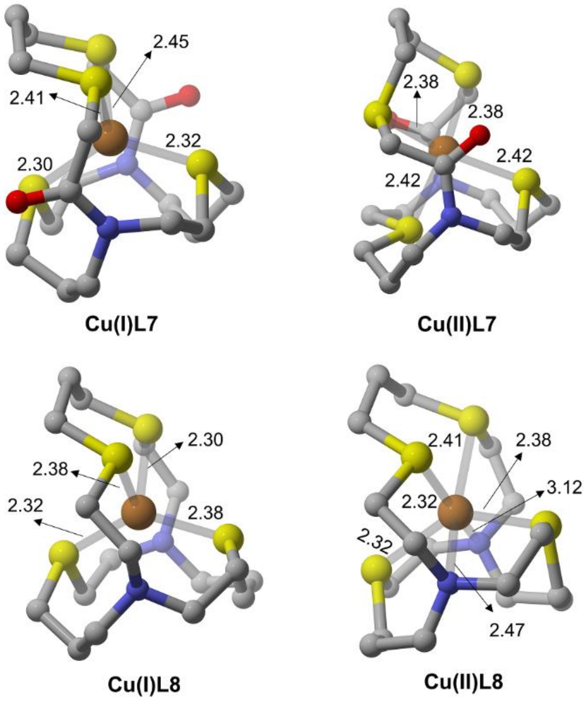

Cu(I)L7

Cu(II)L7

Cu(I)L8

Cu(II)L8

Figure 7 Computed geometries for the lowest-lying copper complexes of L7 and L8.

Table 3 Experimental and computed g-tensors for the lowest-lying conformer (Cu(II)L8) of L8 chelated with Cu(II) ions.

g-tensor	Exp (298 K)	Cu(II)L8
g_1	2.016	2.014
g_2	2.084	2.079
g_3	2.122	2.103
g_{iso}	2.074	2.065

Natural population analysis (NPA)[59-60] was performed on L7 and L8 to understand the preference of L7 for Cu(I). We observed the magnitude of charges on the sulfur atoms to be lower in L7 than L8, thereby making them softer nucleophiles. We postulate the preference of softer nucleophiles by Cu(I), coupled with its inherent stability in acetonitrile (the solvent used for EPR experiments) compared to Cu(II), as the predominant reason for the observed stability of Cu(I) complexes of L7. Furthermore, we observed a longer than usual coordination distance (> 3.0 Å) with one of the nitrogen atoms, resulting in a pseudo five-coordination state for Cu(I) and (II) resembling the metalloenzymes plastocyanin and azurin. Conformers with shorter coordination for the sixth ligand were found to over 2 kcal/mol higher in energy due to steric interactions between the methylene groups of the cryptand backbone. ESP slices were generated to visualize the electrostatic environment inside L7 and L8 surrounding the copper ions. ESP slices for Cu(I) and Cu(II) complexes of L7 and L8 across the plane containing copper, sulfur and nitrogen atoms (Figure 8) revealed strong stabilizing interactions for positively charged ions for the amine cryptand L8, compared to the amide cryptand L7. These results further validate the soft nucleophilic nature of L7 resulting in less stable Cu(II) complexes.

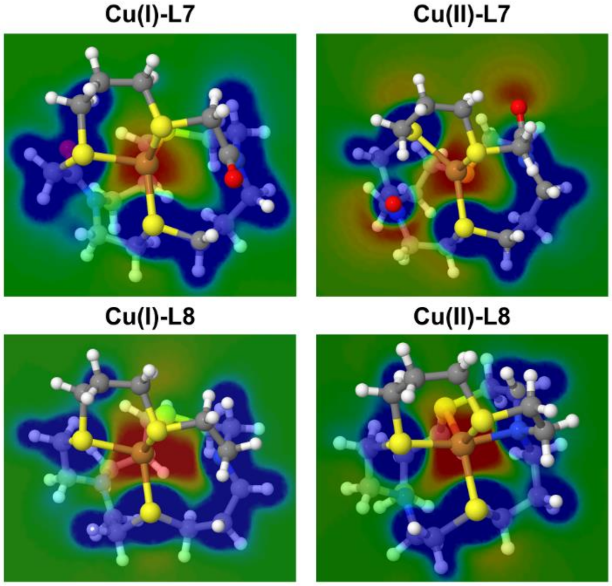

Figure 8 ESP slices generated at ωB97X-D/def2-TZVP level of theory for copper complexes (red = −60 kcal/mol; blue = +60 kcal/mol).

Conclusions

We have used density functional theory methods to elucidate the structure of eight novel aza-thia and tetra thia lactams and cryptands. The lowest-lying conformers for L1, L7, and L8 were found to be in excellent agreement with the X-ray crystallographic structures. Furthermore, we identified a reduction in the N_2S_2 pore size as the bridgehead length was reduced from nine carbons to seven carbons. Bicyclic lactams exhibited two rotameric forms that differ by the relative orientation of the two carbonyl groups. We observed a preference for parallel alignment of the carbonyl groups in bicyclic lactams L1 and L7, while the anti-parallel alignment of carbonyl groups was preferred in L2 and L3. The computed barriers for the rotamer interconversion were found to decrease with decreasing pore size. All the cryptands were found to exhibit three topomers, *viz. in*/*in*, in/out, and out/out based on the orientation of the lone pairs on the nitrogen atoms. The lowest-lying structures for all the cryptands studied showed a strong preference for *in*/*in* topology. These topomers were found to interconvert with a barrier of only 10 kcal/mol. The N_2S_2 core in lactams was found to be more strained than in the corresponding cryptands due to sp^2 hybridized nitrogen atoms in lactams.

Cu(I) and Cu(II) complexes of L7 and L8 were also investigated computationally to elucidate their structures and the coordination state of copper ions. It was observed that copper ions exhibited six coordination, with a longer than average coordination distance for the sixth ligand. This was attributed to the added steric strain of the lactam/cryptand framework.

Computational Methods

An exhaustive exploration of conformational space was performed using the MMFF force field in conjunction with the macrocycle search feature of Schrodinger's Macromodel suite[109] with an energy cutoff of 10 kcal/mol. The geometries of the resulting conformers were then optimized at the B97-D/def2-TZVP level of theory,[17,18, 110] accounting for solvent effects with IEF-PCM[111-112] (using dimethyl sulfoxide as solvent). Geometries, harmonic vibrational frequencies, and thermal free energy corrections (298K) were computed at the same level of theory. Representative transition state (TS) structures connecting selected energy minima were verified by the presence of a single imaginary vibrational frequency. Thermal free energy corrections were based on the quasi-rigid rotor/harmonic oscillator (quasi-RRHO) approximation of Grimme.[113] The final presented free energies were computed at the PCM-ωB97X-D/def2-TZVP//PCM-B97-D/def2-TZVP level of theory.[17,18,110-112, 114] NMR shielding tensor computations were carried out at the IEFPCM-mPW1PW91/6-311G(2*d*,*p*) level of theory[115-117] using the gauge independent atomic orbital (GIAO) method[8, 118] (chloroform as solvent). This level of theory has been shown to be very accurate for predicting ^1H chemical shifts.[9] All the computations were performed using Gaussian 09[119] and the B97-D computations employed density fitting techniques. Molecular structure figures were generated using CYLview.[120]

CHAPTER 3

[18]ANNULENE: A MORE COMPLETE STORY[b]

---

[b] Mallojjala S. C. *et al.* To be submitted to *J. Am. Chem. Soc.*

Abstract

We report computational studies on [18]annulene to address the ground state symmetry, enthalpy of formation, aromaticity, and pathways for inner/outer proton conversion. Zero-point vibrational energy corrected single point computations at the DLPNO-CCSD(T)/cc-pVTZ level of theory on the conformer geometries obtained at the DFT level confirm the symmetry of the effective lowest-lying ground state geometry to be D_{6h}, in contrast to a wealth of recent 'high-level' computational studies. We postulate that the discrepancy noted in earlier computational studies with experimental data is predominantly due to the overestimation of the electronic energy difference between the C_2 and the D_{6h} structures at the CCSD(T)/DZ level of theory. Focal point extrapolated electronic energy difference between the C_2 and the D_{6h} structures further validates this hypothesis. Our computed enthalpy of formation for [18]annulene is 130.8 kcal/mol, thereby resolving the sizeable discrepancy in the literature. Our study also shows that [18]annulene is more polyene in character than benzenoid based on the enthalpy of formation, nucleus-independent chemical shifts, and isomerization stabilization energies. We also report multiple pathways for the inner/outer proton interconversion of [18]annulene. The computed barriers for the lowest-lying pathways and the corresponding interconversion rates are in general agreement with experimental data and suggests that multiple pathways are responsible for this inner/outer proton interconversion.

Introduction

The study of annulenes, long of great theoretical interest, has recently undergone a renaissance. The literature on annulenes is quite extensive and has mostly been summarized in multiple reviews.[121-122] Annulenes may be divided into two classes, *viz*. [4n]annulenes and [4n+2]annulenes. Castro and Karney,[123-127] Rzepa,[128] Allinger,[129-132] Schaefer,[66, 133] and Schleyer,[65-66, 123, 134-136] among others,[67, 137-143] have studied the ground state symmetry, conformational changes, and inner/outer proton interconversion for various [4n] and [4n+2]-annulenes. A central point of contention concerning [4n+2]annulenes is the size at which fully delocalized π-systems give way to poly-ene like character. [18]annulene stands at the center of this debate, since X-ray crystallography yields a bond-equal structure with D_{6h}-symmetry[136, 144-145] while computations support bond-localized ground state structures of either C_2 or D_{3h}-symmetry.[66-67, 131, 143] In 2004, Schaefer, Schleyer and co-workers[66] studied [18]annulene using single point energy computations at CCSD(T)/DZP(C)+DZ(H) level of theory, establishing a C_2-symmetric structure with alternating double and single bonds for the ground state. This was further supported by computed ^{1}H-NMR chemical shifts and the observation of a very large imaginary mode of 1100i cm^{-1} for the non-alternating D_{6h} symmetric structure at the BHandHLYP/6-311+G(d,p) and KMLYP/6-311+G(d,p) levels. The timescale of X-ray crystallographic measurements and insurmountable disorder problems were cited as an explanation for the observed discrepancy with the X-ray geometry.

Recently, Allis and coworkers[67] showed that the aforementioned discrepancy[66-68, 71, 144-147] might be due to the zero-point level sampling of D_{3h}- and C_2-symmetric minima resulting in an effective D_{6h}-symmetric structure, despite the D_{6h}-symmetric stationary point being a saddle-point at the KMLYP/6-311++G(2d,2p) level of theory. However, they suggest that the NMR spectrum of [18]annulene is dominated by the bond localized C_2 symmetric structure. More recently, Kwan and coworkers[68] used quasi-classical dynamics simulations to compute NMR chemical shifts for [18]annulene, observing that chemical shifts corresponding to the D_{6h} and D_{3h} symmetric structures are in closer agreement with experiment than those of lower symmetry. Despite these efforts, a thorough understanding of the ground state symmetry of [18]annulene is still lacking. This can be attributed in equal measure to a lack of experimental data owing to the synthetic challenges involved, the stability of [18]annulene, and a lack of rigorous computational study across different functionals and basis sets. Despite the synthetic challenges, the X-ray crystal structure[136, 144-145] of [18]annulene has been reported multiple times. For fluxional molecules like [18]annulene, which undergo substantial conformational changes, the experimental structures provide a time-averaged structure. Since computations are capable of revealing a single point on the potential energy surface, it is possible to gain insight into selected points on the potential surface with more certainty. This gives computational methods a powerful advantage over experimental methods.

In this work, we have determined as much of the potential energy surface as we believe to be of current interest to address the conformational and the ground state symmetry problem. For clarity, and owing to the tendency of many computational methods to predict minescule deviations from exact point group symmetry for many stationary points on the [18]annulene potential energy surface, we focus on the broad question of whether the ground state is a planar bond equal structure (1) or a non-planar bond alternating structure (2).

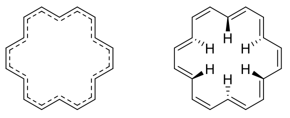
1

2

Scheme 4. Potential low-lying structures of [18]annulene. The planar non-alternating form (1), and the non-planar form with alternating bond lengths (2).

Schleyer and Wannere[65] reported isomerization stabilization energy and nucleus independent chemical shifts[134] (NICS) to characterize the degree of aromaticity of the D_{6h} structure of [18]annulene. However, thermodynamic stability as an alternative measure of aromaticity hasn't been explored for [18]annulene. Unfortunately, there is a significant discrepancy in the experimental values for the enthalpy of formation, a measure of thermodynamic stability, for [18]annulene. In 1965, Sondheimer and coworkers[69] reported a value of 67±6 kcal/mol for the enthalpy of formation based on combustion experiments. Nine years later, Oth and coworkers[70] reported a value of 124±5.5 kcal/mol, thereby establishing a need for a more accurate value of the enthalpy of formation for this system. Strangely, we were unable to find any modern computational study aimed at resolving this discrepancy.[132, 143]

At low temperatures, [18]annulene exhibits distinct ^{1}H NMR chemical shifts for the inner and outer protons. However, Oth *et al.*[71] reported that these peaks coalesce at 314K and only a single sharp peak is visible at temperatures exceeding 394 K, indicating relatively rapid interconversion of the inner/outer protons. Oth proposed that at elevated temperatures the three degenerate [18]annulene structures (1, 1′, *etc.*) interchange via the formal pathway depicted in Scheme 5, thereby causing the peaks to coalesce. Starting from the planar bond equal structure 1 (presumed to be an energy minimum by Oth), this pathway involves first the localization of π-bonds followed by the rotation of three C=C bonds, a bond-shift passing through a D_{3h}-symmetric intermediate, and then three more rotations around C=C bonds before yielding the equivalent bond equal structure. Analyses of the variable temperature NMR data provided an enthalpic barrier of 16.1 kcal/mol for this inner/outer proton interconversion.[71] This pathway has not been studied computationally and there are possible alternative pathways depending on the precise order of different C–C bond rotations and bond shifts that were not considered viable by Oth and co-workers.[71] Furthermore, Castro and Karney[125] showed that a similar dynamic inner/outer proton interconversion occurs in [12]-annulene via a transition state with Möbius topology, suggesting that the interconversion of inner/outer protons in [18]annulene could also involve a Möbius-like pathway. However, a Möbius-like TS or intermediate for [18]annulene would be antiaromatic, so is likely disfavored relative to the pathway proposed by Oth.[71, 148]

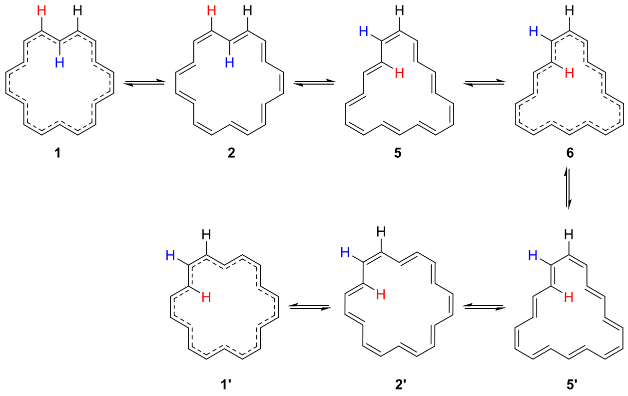

Scheme 5. Oth's formal pathway for inner/outer proton interconversion.[71]

Herein, we report geometries, energies, enthalpy of formation and isomerization stabilization energies (ISE) for [18]annulene using DFT and robust ab initio methods. We also report detailed studies to identify the predominant pathways for inner/outer proton interconversion in [18]annulene.

Results and Discussion

Ground State Structure

The potential energy surface surrounding the D_{6h}-symmetric stationary point for [18]annulene is exceptionally sensitive to level of theory. We examined the D_{6h}-, D_{3h}-, and C_2-symmetric structures using a number of popular DFT functionals paired with both the 6-311+G(d,p) and def2-TZVP basis sets. Different functionals give highly variable results. For instance, ωB97X-D/def2-TZVP indicates that the D_{6h}-symemtric structure is a fourth order saddle point, while the quasi-planar D_{3d}-symmetric version is a first order saddle point. B3LYP/def2-TZVP predicts a first-order saddle point for the D_{6h}-symmetric geometry, while this same functional paired with 6-311+G(d,p) predicts the D_{6h}-symmetric structure of [18]annulene to be an energy minimum. The D_{3h}-symmetric structure, which Hudson and Allis[67] found to be an energy minimum at the KMLYP/6-311++G(2d,2p) level of theory, was found to be a bond-equal first order saddle point. Upon examining the geometries closely, the D_{6h}, and planar D_{3h} structures differ minimally from one another. Based on these results, we have opted to not classify the ground state of [18]annulene based on the symmetry of the system, but instead focus on the more pertinent question of a planar, bond-equal or non-planar, bond-alternating ground state.

To establish a DFT method that provides the most reliable conformational energies for [18]annulene, we computed geometries for nine low-lying structures (see Figure 8) using six DFT functionals paired with two basis sets and compared these to results at the DLPNO-CCSD(T)/cc-pVTZ level of theory. Electronic energies relative to the bond-localized structure 2 using selected functionals as well as DLPNO-CCSD(T) are listed in Table 4. DLPNO-CCSD(T) predicts that structure 2 is lowest-lying, falling 1.6 kcal/mol lower in electronic energy than structure 1; the other conformers are all at least 2.8 kcal/mol higher in energy than structure 2. Overall, the ωB97X-D/def2-TZVP method provides highly accurate relative energies for these conformers, closest match with the reference DLPNO-CCSD(T) data, apart from over-estimating the energy of 1 relative to 2. Notably, the energies from ωB97X-D appear to be far more accurate than those of KMLYP, which has been previous used for this systems.[66]

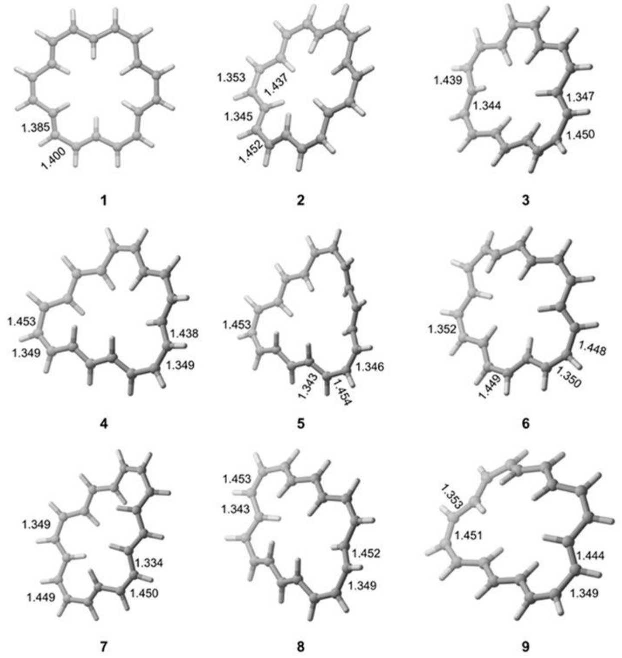

Figure 9 Computed low-lying structures of [18]annulene at the ωB97X-D/def2-TZVP level of theory.

Among the conformers in Figure 9, structure 1 has two nearly equal bond lengths (1.385 and 1.400 Å) while structures 2-9 showed a strong tendency towards alternating bond lengths (1.445±0.007 and 1.350±0.005 Å). Moreover, structure 1 was planar while structures 2-9 were non-planar. Efforts to obtain planar minima for 2-9 were unfruitful. These results demonstrate the benzenoid nature of 1 and polyene like nature of 2. To obtain more accurate geometric parameters for 1, we performed a DLPNO-CCSD(T)/cc-pVTZ geometry optimization *via* the method of finite differences. Geometric parameters obtained through this optimization were in excellent agreement with the X-ray crystallographic measurements[144-145, 147]. A similar optimization for 2 couldn't be performed owing to the increased number of degrees of freedom.

Table 4. Relative electronic energies (in kcal/mol) for different structures of [18]annulene.[a]

Structure	B3LYP	wB97X-D	BH&HLYP	DLPNO-CCSD(T)
1	0.0	4.7	2.5	1.6
2	0.0	0.0	0.0	0.0
3	5.1	3.0	3.7	2.8
4	6.1	2.3	3.6	2.4
5	7.9	3.3	5.0	3.4
6	9.4	7.4	8.1	7.2
7	5.7	2.0	3.5	2.4
8	6.7	2.2	4.1	2.4
9	7.1	3.9	5.1	4.0

[a] B3LYP and BHandHLYP (BHLYP) computed with 6-311+G(d,p) and ωB97X-D computed with the def2-TZVP basis set; DLPNO-CCSD(T) energies computed with the cc-pVTZ basis set at the ωB97X-D/def2-TZVP optimized geometries.

While the DLPNO-CCSD(T) computations clearly predict structure 2 to be lower in electronic energy than structure 1, this energetic ordering switches upon inclusion of zero-point vibrational energy corrections. This is true regardless of which DFT functional is used to predict vibrational frequencies. As noted by Allis and coworkers,[67] for the commonly used BHandHLYP/6-311+G(d,p) level of theory, the electronic energy surface was found to be a double well potential. However, a qualitative investigation of the DLPNO-CCSD(T)/cc-pVTZ electronic energy surface surrounding structure1 indicated it to be a minimum, thereby suggesting that it might not be a double well potential but a more complex toplogy. This, along with data from Table 4, further illustrates the sensitivity of the potential energy surface of [18]annulene to the level of theory employed. We postulate this functional and basis set sensitivity to be due to an incomplete capture of the electron correlation energy. Moreover, the discrepancy between this work and past computational efforts[66] can mainly be attributed to the overestimation of the electronic energy difference between structures 1 and 2 by the past studies, which is a direct consequence of the incomplete capture of electron correlation energy at lower basis sets.

To further validate these results and support our assertion, we performed an incremental focal point analysis[149-151] to obtain the electronic energy difference between 1 and 2 at the complete basis set limit and to examine the qualitative behavior of electron correlation energy. The focal point extrapolated value for the electronic energy at the complete basis set limit was obtained to be 1.4 kcal/mol, favoring 2. Furthermore, electron correlation energy was found to favor structure 1, which resulted in a decrease of the electronic energy difference between 1 and 2 from 2.1 kcal/mol at the cc-pVDZ basis set to 1.4 kcal/mol at the complete basis set limit. Upon ZPVE correcting this energy, we find that structure 1 is favored over structure 2 by 0.5 kcal/mol, thereby confirming the ground state of [18]annulene as a bond-equal structure, in agreement with the X-ray crystallographic data.[144-145, 147] Thus, while the vibrationally averaged structure is a planar, bond-equal structure (1), the general flatness of the surrounding potential energy surface will result in significant bond-alternating character, explaining the polyene-like reactivity of [18]annulene.[147]

Aromatization energy and enthalpy of formation

We then proceeded to evaluate the aromatic nature of [18]annulene with respect to benzene. HOMA indices were computed for structure 2 of [18]annulene and of benzene to gain insights into the aromatic nature of [18]annulene (see Table 5). HOMA analysis suggests that [18]annulene is far less aromatic than benzene. Furthermore, the aromatic stabilization energy (ASE) was assessed using the method of isomerization stabilization energy (ISE). This was done at the DLPNO-the CCSD(T)/cc-pVTZ//ωB97X-D/def2-TZVP level of theory. A strain balanced scheme (see Scheme 6) was used to evaluate the ISE. An ISE value of 10.1 kcal/mol was obtained for 2 while an ISE of 31.2 kcal/mol was obtained for benzene, again indicating that 2 is significantly less aromatic and more polyene-like than benzene.

Table 5 Computed aromatic indices for compounds 1 and benzene.

Index	2	Benzene	%Benzenoid character of **2**
HOMA	0.4	1.0	40
ISE (kcal/mol)	10.1	31.2	32
NICS (ppm)	-5.5	-9.7	N/A
ΔH°_f(298K) (kcal/mol)	130.8	18.5	42

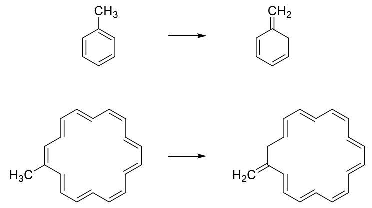

Scheme 6. Strain balanced equations used to compute ISE.

To further validate this result, we computed the enthalpy of formation at the same level of theory for benzene and [18]annulene, as aromatic systems have lower per carbon enthalpies of formation. The homodesmotic equation[54] from Scheme 7 was used to compute the enthalpy of formation. We obtained an enthalpy of formation of 130.8 kcal/mol for 2 as opposed to that for benzene, which was computed to be 18.5 kcal/mol. This enthalpy of formation for 2 was found to be significantly higher than three times the enthalpy of formation of benzene, further validating that 2 is more polyene like than "truly aromatic". Computed nucleus independent chemical shifts (NICS) for 2 and benzene (Table 5) further demonstrate that 2 has much lower aromaticity than benzene.

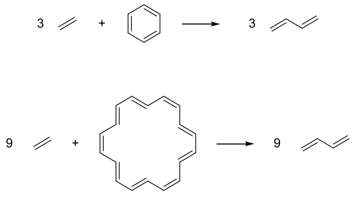

Scheme 7. Homodesmotic equations used to compute the enthalpy of formation for benzene and [18]annulene.

Inner/outer proton interconversion

Twenty-four pathways were evaluated to investigate the inner/outer proton interconversion of [18]annulene. Of these, 23 involved rotations across C-C=C-C bonds, differing by the order of bond rotations and bond shifts, while the remaining pathway passed through a Möbius-like TS geometry analogous to that computed for [12]-annulene by Castro and Karney.[125] All the pathways identified were verified by performing IRC calculations. We find that while Oth's proposed pathway[71] is relatively low-lying, there is one pathway that has a more favorable activation energy (see Scheme 8). In this most favorable pathway, starting from structure 2 there is a bond rotation to form 3, followed by a bond-shift to form 3s. This is followed by two bond rotations to form 8 then 9, then another bond shift to form 9s. From here, the opposite order is followed, eventually leading to structure 2'. Overall, in contrast to Oth's formal pathway, there are three bond shifts interspersed among the six bond rotations. The highest barrier for this process is the initial conversion from structure 2 to 3, resulting in an enthalpy of activation that is ~1 kcal/mol lower that of Oth's proposed pathway.[71] However, given the energetic proximity of these two pathways, they are both likely to be operative at elevated temperatures at which inner/outer proton conversion is observed. Including ZPVE corrections, the barrier for this interconversion at the DLPNO-CCSD(T)/cc-pVTZ//ωB97X-D/def2-TZVP level of theory was found to be 12.4 kcal/mol (Figure 10) for the lowest-lying pathway, which is lower than the experimental enthalpic barrier of 16.1 kcal/mol reported by Oth.[71]

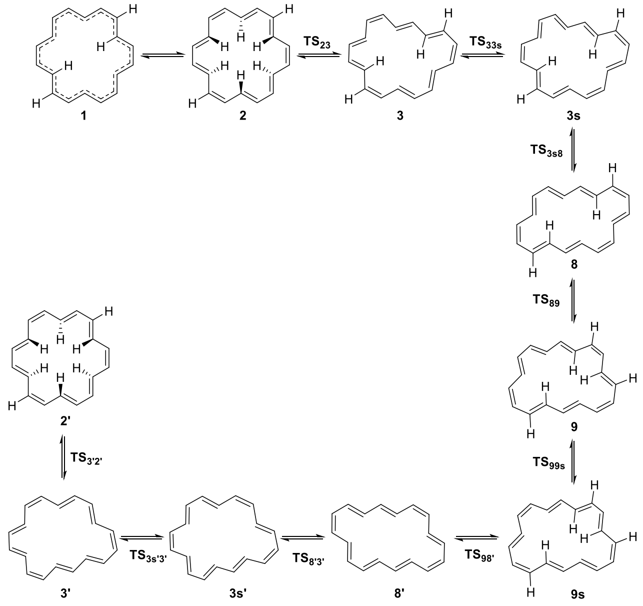

Scheme 8. Schematic representation of the computed lowest-lying pathway for inner/outer proton conversion in [18]annulene.

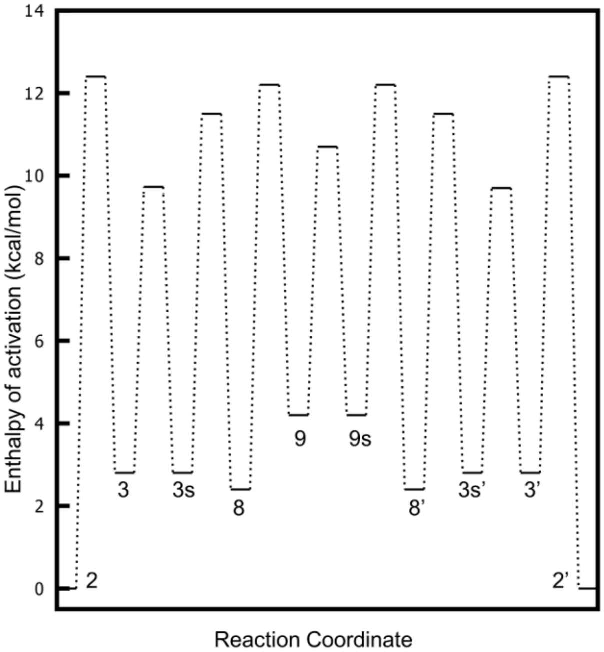

Figure 10 DLPNO-CCSD(T)/cc-pVTZ//ωB97X-D/def2-TZVP ZPVE corrected potential energy surface for the lowest-lying pathway for inner/outer proton interconversion in [18]annulene.

Conclusions

We have used 12 DFT levels of theory and DLPNO-CCSD(T)/cc-pVTZ *ab initio* energies to study various conformers of [18]annulene to establish the symmetry of the lowest-lying conformer. The nature of the low-lying D_{6h}- and C_2-symmetric stationary points is exquisitely sensitive to level of theory, which underlies the disparate findings of previous computational studies. In agreement with some recent computational work,[66] we find that the C_2-symmetric stationary point is the global minimum energy on the electronic energy surface. However, as suggested by Allis and co-workers,[67] we find that the D_{6h}-symmetric stationary point is the global minimum on the ZPVE corrected surface. We cannot say with certainty whether this stationary point is an energy minimum or a first-order saddle point. Regardless, the effective structure of [18]-annulene, even at 0K, has D_{6h}-symmetry. This is in accord with experiment.[71, 144-147] The discrepancy between the experimental and past computational works can be attributed to an overestimation of the electronic energy of the D_{6h} stationary point relative to the C_2-symmetric structure for [18]annulene in the computations due to the use of small basis sets. We report an accurate computed value for the enthalpy of formation of [18]annulene of 130.8 kcal/mol, thereby resolving the discrepancy in the literature.[69-70] Finally, we identify a new low-lying pathway for the inner/outer proton interconversion in [18]annulene. Our computed enthalpic barrier of 12.4 kcal/mol, albeit lower than the experimental barrier reported by Oth,[71] qualitatively agrees with the experimental hypothesis of the presence of multiple pathways in the inner/outer proton interconversion of [18]annulene. Overall, our data indicates that two nearly independent dynamical processes are occurring for [18]annulene. On a short timescale, the molecule undergoes an inversion process between the two C_2 symmetric structures even at 0K. On longer timescales, the inner/outer interconversion occurs via multiple pathways. Both theory and experiments[71] are consistent with the hypothesis that the inner/outer proton flipping in [18]annulene occurs via rotation about multiple C-C=C-C bonds.

Computational Methods

Density functional theory was employed for geometry optimizations, identifying transition states, and computing vibrational frequencies using Gaussian 09.[119] Common DFT functionals including B3LYP,[152] B97-D,[153-154] ωB97X-D,[114] M06-2X,[155] BH&HLYP,[156-158] KMLYP[159] were used with the 6-311+G(d,p)[117] and def2-TZVP[110] basis sets. Single point energies were computed at the DLPNO-CCSD(T)/cc-pVXZ[160-163] (X = D, T, Q) level of theory for selected geometries and at the DLPNO-CCSD(T)/cc-pVTZ level of theory for all structures using ORCA.[164] All the transition states were verified by the presence of one imaginary vibrational mode. The method of finite differences was used to optimize a D_{6h} symmetry structure of the ground state at the DLPNO-CCSD(T)/cc-pVTZ level of theory (See SI). ^{1}H NMR chemical shifts and NICS were computed using GIAO-B3LYP/6-311+G(d,p) as suggested by previous studies.[118] Enthalpies of formation of the references species in Scheme 7 were obtained from ATcT database.[165] Harmonic oscillator model of aromaticity (HOMA)[166-167] indices were computed at the ωB97X-D/def2-TZVP level of theory.

CHAPTER 4

ROLE OF ALKALI METALS IN CHIRAL PHOSPHORIC ACID CATALYSIS[c]

---

[c] Mallojjala S. C. *et al.* To be submitted to *ACS Cat*.

Abstract

Chiral phosphoric acids (CPA) derived from chiral diols (*e.g.* BINOL) have gained prominence as privileged scaffolds for organocatalytic transformations. Ishihara and coworkers[76] demonstrated the potential utility of alkaline earth metal salts of CPAs (CMPs) as catalysts for Mannich type reactions of aldimines. Subsequent reports have demonstrated a marked difference in stereoselectivity between such metal phosphates and their corresponding CPAs. Paton and coworkers[168] postulated the geometric differences in the steric environment of CMPs to be responsible for the stereo reversal observed by Ishihara and coworkers. However, recent reports by Antilla and coworkers[77] have identified stereo reversal in alkali metal phosphate catalyzed reactions compared to their corresponding CPAs despite having a geometrically similar chiral pocket. The desymmetrization of *meso*-epoxides was chosen as a suitable example to understand the activity and origin of selectivity in chiral metal phosphate catalyzed reactions. In the case of epoxide desymmetrization catalyzed by CMPs, the metal ion of the chiral phosphate activates the epoxide by bonding with the oxygen, thereby facilitating the attack of the nucleophile. Analyzing the transition states (TSs) for the thiolysis of epoxides suggested that the interactions between metal phosphate and epoxide are the key factors governing the selectivity. Further decomposition of this interaction energy using energy decomposition approaches identified the perturbations caused by the metal ion to the electrostatic environment of the epoxide in the stereocontrolling TS structures as important. These results pinpoint electrostatic effects induced by the presence of the metal ions as a reason for the difference in stereoselectivity between metal phosphates and CPAs.

Introduction

Chiral phosphoric acids (CPAs) have gained prominence as versatile organocatalysts for stereoselective transformations.[19, 23, 26, 29, 72-73] Traditionally, CPAs were used as bifunctional Bronsted acid catalysts and the activity of these catalysts was mainly attributed to the steric interactions of the 3,3' substituents[23, 72-73, 169-172] and pK_a.[74, 173] However, experimental and computational studies by Jacobsen,[56-57] Sigman,[53, 174-175] Toste,[53, 175] Sunoj,[26, 176-178] and Wheeler,[19, 29, 49-51, 179] among others,[15, 180-182] have identified the interplay between steric interactions and the numerous non-covalent interactions between the substrates and the catalyst as the source of selectivity in many CPA-catalyzed reactions. Exploiting these subtle interactions has resulted in improvements in stereoselectivity and activity of previously studied CPA-catalyzed reactions and paved the way for the development of novel CPA-catalyzed stereoselective transformations. Despite these advantages and developments, CPAs are readily neutralized to their respective alkali and alkaline earth metal salts by purification on silica gel. Ding and coworkers[75] demonstrated that by performing an acid purification of these CPAs, the efficacy of the catalysts can be increased. Furthermore, Rueping and coworkers[74] eliminated calcium salts of CPAs as active catalytic species for an organocatalyzed carbonyl-ene reaction. These results demonstrated the detrimental effects of chiral metal phosphate impurities (CMPs) to activity and stereoselectivity in some CPA-catalyzed reactions. However, Ishihara and coworkers[76] reported stereo reversal with chiral alkaline earth metal phosphate catalyzed asymmetric Mannich reaction compared to its CPA-catalyzed counterpart (see Scheme 9). This discovery led to the emergence of chiral metal phosphate catalysis, and efforts from the Antilla,[77, 183-186]

Nakamura,[187] Della Sala,[188] and Rajanbabu[79] groups has furthered the field of chiral alkali and alkaline earth metal phosphate catalyzed asymmetric synthesis.

Despite these experimental advances, the role played by alkali and alkaline earth metals in these systems and the cause for stereo reversal with respect to parent CPAs is poorly understood. Recent efforts by Paton and coworkers[168] on Ishihara's Mannich reaction catalyzed by CMPs and CPAs (Scheme 9) shed light on the underlying role played by alkaline earth metals. Paton *et al.*[168] identified the geometric differences in the chiral pocket between CPAs and calcium bis-CMPs to be the reason for the observed stereo reversal in their study. Furthermore, they also reported a difference in coordination number between calcium and magnesium as a predominant reason for the selectivity difference observed despite having geometrically similar chiral pockets.

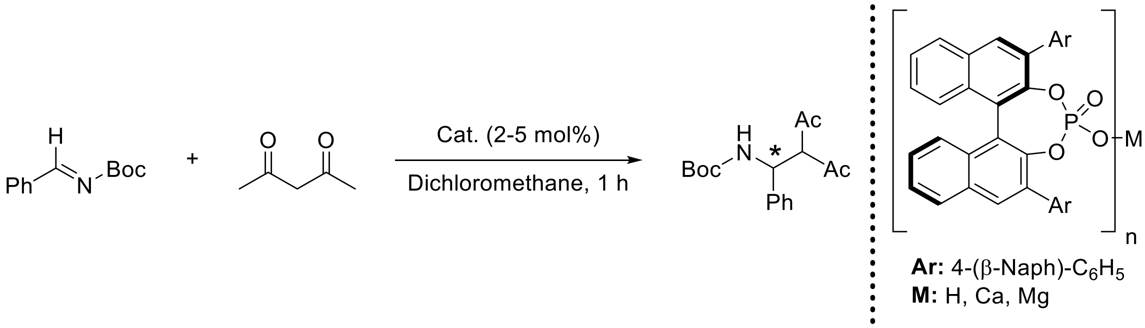

Scheme 9 An asymmetric Mannich reaction reported by Ishihara and coworkers.[76]

Table 6 Enantioselectivity data reported by Ishihara and coworkers[76] for an asymmetric Mannich reaction.

M	Major enantiomer	Experimental ee (%)
H	S	27
Ca	R	92
Mg	R	43

However, no studies exist for the chiral alkali metal phosphate analogues of CPAs where, despite the chiral pocket being geometrically equivalent to that of CPAs, a reversal in stereoselectivity was observed. One such example is the CPA-catalyzed epoxide desymmetrization reaction in the presence of thiols reported by Sun *et al*.[189] (R1, Scheme 10) and its CMP catalyzed counterpart reported by Antilla and coworkers (R2-R4, Scheme 10).[77] Seguin *et al*.[49] and Ajitha *et al*.[190] independently studied reaction R1 using modern DFT methods and identified numerous non-covalent interactions as the key factor for the observed selectivity. Furthermore, both studies identified the strength of CH···O interactions between the epoxide and phosphoryl oxygen as a key factor for the observed selectivity. Seguin *et al*.[49] proposed an electrostatic model to explain the general selectivity trend observed in CPA-catalyzed epoxide desymmetrization reactions and compared it to an enzyme catalyzed reaction.

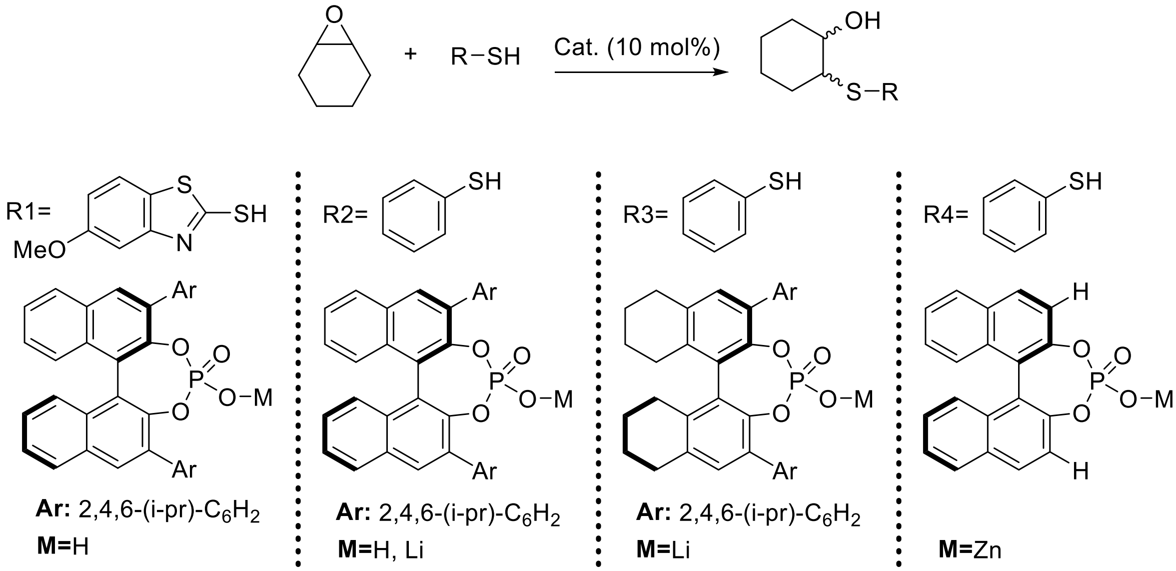

Scheme 10 Epoxide desymmetrization reaction catalyzed by CPA and various CMPs.

Table 7 Experimental enantioselectivity data for various CPA and CMP catalyzed epoxide desymmetrization reactions.

Reaction	Major enantiomer	Yield (%)	Experimental ee (%)
R1 (M=H)	(R,R)	98	61
R2 (M=H)	N/A	0	0
R2 (M=Li)	(S,S)	92	83
R3 (M=Li)	(S,S)	97	91
R4 (M=Zn)	(S,S)	93	60

No computational studies exist for reactions R2-R4. Moreover, Antilla and coworkers[77] observed no desymmetrization products with the commonly used CPA TRIP [R2 (M=H), Table 7] and stereoselectivity was retained in R4 despite lacking any sterically demanding 3,3’ substituents. Herein, we report computational studies on several CMP catalyzed epoxide desymmetrization (R2-R4, Scheme 10) using modern

DFT methods. Furthermore, we investigated the role played by alkali metal in stereo reversal compared to previous computational studies on R1 by Seguin *et al*.[49]

II. Results and Discussion

Macromodel,[109] a molecular mechanics package, was used to identify the lowest-lying conformers for each of the catalysts and reactants. These conformers were then combined exhaustively to generate initial structures for transition state (TS) optimizations. The stereocontrolling step was identified to be a concerted S_N2-like TS depicted in Figure 11. The lowest-lying TS structures for R2 with M as lithium are shown in Figure 11 with the epoxide bound to the catalyst via the lithium ion. For reactions R3 and R4, the lowest-lying structures were found to be structurally similar to R2 with lithium. However, for reaction R2 with hydrogen, the lowest-lying TS structures resembled that of reaction R1 previously reported by Seguin *et al*.[49] These structures can be found in Appendix C Figure 20. In all of the reactions, the S_N2-like attack of the nucleophile is accompanied by the deprotonation of the nucleophile by the phosphoric acid.

Computed relative free energy barriers and enantiomeric excess (*ee*) values are shown in Table 8 and are found to be in agreement with experiment. In particular, even though the selectivity is slightly over-predicted, the trend in enantioselectivities were captured accurately. For comparison, we also recomputed the TS structures for reaction R1 using the same level of theory used for R2-R4. For reaction R2 with M as hydrogen, computed enantiomeric excess was used to understand the stereoselectivity with a CPA catalyst for thiophenol as the nucleophile. We predict CPA-catalyzed R2 reaction to provide the same stereoselectivity as the CPA-catalyzed R1 reaction.

Table 8 Experimental and Boltzmann weighted computed free energy differences for the competing enantiomers for epoxide desymmetrization reactions reported in Scheme 10 in kcal/mol.

Reaction	Experimental $\Delta\Delta G^{\ddagger}$	Major enantiomer	Computed $\Delta\Delta G^{\ddagger}$
R1 (M=H)	0.8	(*R*,*R*)	1.0
R2 (M=H)	N/A	(*R*,*R*)	1.1
R2 (M=Li)	1.4	(*S*,*S*)	1.8
R3 (M=Li)	1.8	(*S*,*S*)	2.2
R4 (M=Zn)	0.8	(*S*,*S*)	1.5

For all of the reactions investigated, the lowest-lying (*S*,*S*) and (*R*,*R*) TS geometries were very similar to each other, differing only in the position of the nucleophile. The lowest-lying TS structures for reaction R2 (M=Li) are shown in Figure 11. The lowest-lying TS structure leading to the major enantiomer is favored by 1.8 kcal/mol over the lowest-lying TS structure leading to the minor enantiomer on the Gibbs free energy surface and by 2.4 kcal/mol on the electronic energy surface. The S-H···O distance is smaller in the TS structure leading to the major enantiomer, while the forming bond between the nucleophile and electrophilic carbon of epoxide is shorter in the TS structure leading to the minor enantiomer (see Figure 11).

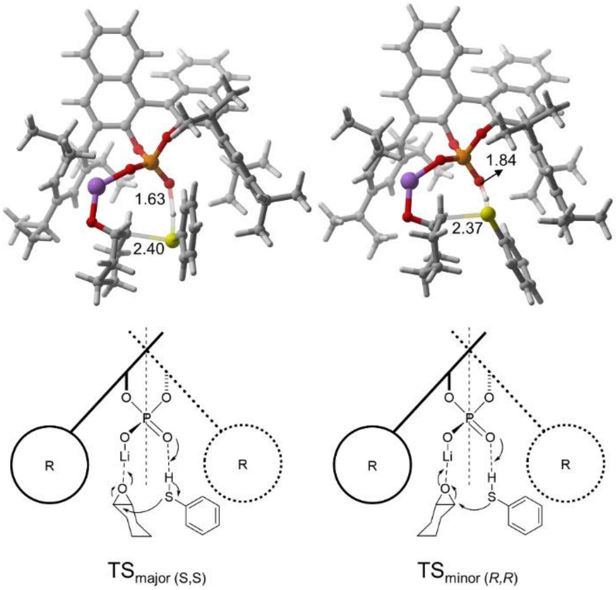

Figure 11 Computed lowest-lying TS structures for a Li-BINOL phosphate catalyzed epoxide desymmetrization reaction (R2 with M as lithium in Scheme 10).

Owing to this structural similarity between the competing lowest-lying TS structures, we employed Houk and Bickelhaupt's[31-35] distortion-interaction/activation-strain model to gain insights into the origin of stereoselectivity. In particular, the barrier heights for lowest-lying TS structures leading to the major and minor products for reaction R2 (M=Li) (see Figure 12) were found to be 16.3 kcal/mol and 18.7 kcal/mol respectively. Upon decomposing these barriers into their respective distortion and interaction components (see Figure 12), the distortion of the reactants is found to be equivalent while the catalyst distortion differs by 1.6 kcal/mol. This, combined with the 0.9 kcal/mol difference in interaction energies, leads to the total reaction barrier difference of 2.4 kcal/mol.

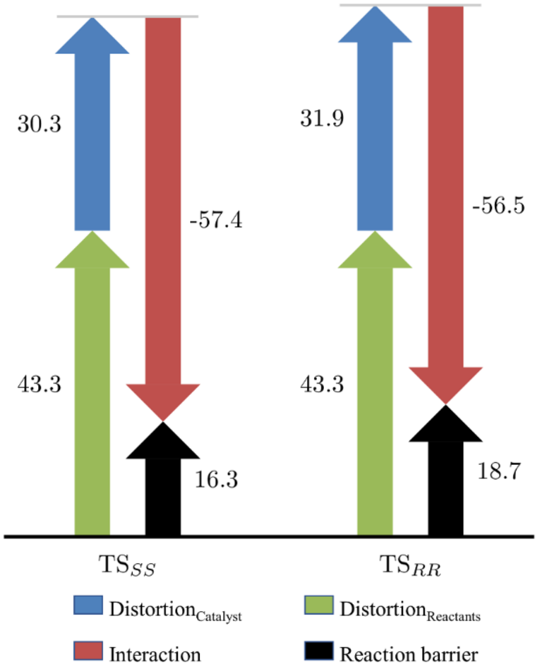

Figure 12 Distortion-interaction analysis for the lowest-lying TS structures shown in Figure 10 for the reaction R2 with M=Li (Scheme 10), in kcal/mol.

Similar analyses were carried out for R1 and R2 (M=H), the latter of which was compared with R2 (M=Li) to understand the origin of stereo reversal. The distortion-interaction contributions to the energy of the TS leading to the minor products, relative to that leading to the major products, for reactions R1, R2 (M=H), and R2 (M=Li) are summarized in Table 9. Geometrically, TS structures leading to the major (*R*,*R*) enantiomer were found to be more distorted than the TSs leading to the (*S*,*S*) enantiomer. This result suggests that the observed stereo reversal is not due to geometric differences in the chiral pocket. Moreover, the magnitude of the interaction energy was found to determine the stereoselectivity.

Table 9 Distortion-interaction data for lowest-lying TSs for selected reactions from table 8 for (*R*,*R*) with respect to (*S*,*S*) in kcal/mol.

Reaction	Enantiomer	$\Delta\Delta E^{\ddagger}$	$\Delta\Delta E_{Distortion}$	$\Delta\Delta E_{Interaction}$
R1 (M=H)	(*R*,*R*)	-2.0	2.1	-4.1
R2 (M=H)	(*R*,*R*)	-1.1	1.5	-2.6
R2 (M=Li)	(*R*,*R*)	2.4	1.6	0.8

We then decomposed the interaction energy into its components to gain further insight. First, we computed the strength of dispersion interactions ($E_{Dispersion}$) between the catalyst fragment and the reactants using Grimme's[191] DFT-D3 approach. Then, the electrostatic component of the interaction energy ($E_{Electrostatic}$) was estimated using Lu and Wheeler's[42-45] approach for quantifying electrostatic interactions. Finally, the leftover component from the interaction energy (E_{ERCT}) was used as an estimate for exchange-repulsion and charge-transfer interactions between the catalyst and the reactant fragments. The relative interaction energy components with respect to (*S*,*S*) enantiomer for the reactions from Table 9 are summarized in Table 10.

Table 10 Energy decomposition analysis for the reactions from table 9 for (*R*,*R*) with respect to (*S*,*S*) in kcal/mol.

Reaction	Enantiomer	$\Delta\Delta E_{Interaction}$	$\Delta\Delta E_{Dispersion}$	$\Delta\Delta E_{Electrostatic}$	$\Delta\Delta E_{ERCT}$
R1 (M=H)	(*R*,*R*)	-4.1	0.4	-2.1	-2.4
R2 (M=H)	(*R*,*R*)	-2.6	0.4	-1.8	-1.2
R2 (M=Li)	(*R*,*R*)	0.8	0.8	1.7	-1.6

Dispersion interactions between the catalyst and the reactants were found to slightly favor the minor enantiomer and electrostatic interactions between the catalyst and reactant fragments were found to strongly favor the major enantiomer in all the cases. Based on these results, we hypothesize the changes in electrostatic environment of the chiral pocket as the predominant reason for the observed stereo reversal in the reaction R2 (M=Li) with respect to the reactions R1 and R2 (M=H). To further investigate the origin of these electrostatic effects, we examined electrostatic potential energy slices across the epoxide and the nucleophile for R2 with M=H and M=Li (see Figure 13).

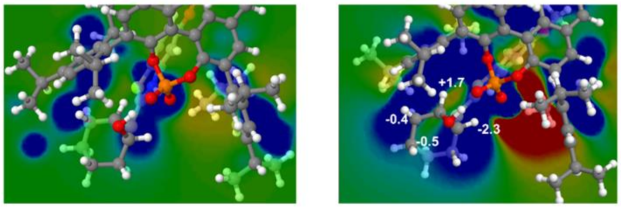

R1 (M=H) $\mathrm{TS}_{\mathrm{major}}$(*R*,*R*) R1 (M=H) $\mathrm{TS}_{\mathrm{minor}}$(*S*,*S*)

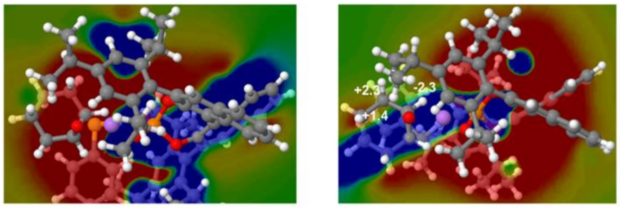

R2 (M=Li) $\mathrm{TS}_{\mathrm{major}}$(*S*,*S*) R2 (M=Li) $\mathrm{TS}_{\mathrm{minor}}$(*R*,*R*)

Figure 13 ESP slice along the plane containing a key C-H…O interaction previously reported by Wheeler *et al.*[49] for the reaction R1 (M=H).

ESP slices coupled with the electrostatic component of the interaction energy revealed strong electrostatic perturbations caused by the alkali metal ion on the epoxide as a primary source for the observed electrostatic effects. Furthermore, the CH···O interactions previously identified to play a key role in the determining the stereo selectivity by Seguin and coworkers[49] were found to be quenched due to the strong perturbations caused by the presence of alkali metal. A similar analysis carried out on the (*R*,*R*) enantiomer for R2 (M=Li) reaction with shorter SH···O distances revealed strong destabilizing electrostatic interactions on the epoxide due to the catalyst. The minor enantiomer with a comparable SH···O distance to that of the major enantiomer was disfavored electrostatically by over 4 kcal/mol. These results together demonstrate the importance of electrostatic perturbations caused by alkali metals in CMP catalyzed reactions in determining the stereoselectivity.

Conclusions

We used modern DFT computations to investigate the role played by alkali metal ions in chiral alkali metal phosphate catalysis and the origin of stereo reversal in CMP catalyzed reactions compared to their CPA-catalyzed counterparts. We identified a lithium BINOL phosphate catalyzed epoxide desymmetrization reaction as a suitable candidate to investigate the role played by Li^+ in determining the stereoselectivity. We used an energy decomposition approach on the lowest-lying TSs to understand the origin of stereo selectivity in both CMP and CPA-catalyzed reactions. Distortion-interaction analysis revealed the geometrical similarities between the chiral pockets of the catalysts studied. Decomposing the interaction energy into its components revealed electrostatic interactions between the catalyst and the reactant fragments as the origin of stereo selectivity. Furthermore, strong electrostatic perturbations by the alkali metal ion on the epoxide were identified as the origin for these favorable electrostatic interactions using ESP slices. This result has further established the importance of non-covalent interactions in organocatalysis.

Computational Methods

Geometries, vibrational frequencies, and thermal free energy corrections were computed at the B97-D/def2-TZVP level of theory,[110, 154, 192] accounting for solvent effects with PCM (the solvent was toluene).[111, 193] Transition state structures were verified by the presence of a single imaginary vibrational frequency. The presented theoretical free energy differences ($\Delta\Delta G^{\ddagger}$) correspond to the difference in free energy between the lowest-lying (*S*,*S*) and (*R*,*R*) transition states for each reaction/catalyst combination based on an extensive search of possible conformations of the catalyst and substrates. It is assumed that these reactions are under Curtin-Hammett control and that the enantioselectivity is dictated by $\Delta\Delta G^{\ddagger}$ for the stereocontrolling step (*vide supra*). Thermal free energy corrections were based on the quasi-rigid rotor/harmonic oscillator (quasi-RRHO) approximation of Grimme.[194] In the quasi-RRHO approach, the entropic contributions of low-frequency vibrational modes are interpolated between the values of a harmonic oscillator and an effective rigid rotor.[195] The final presented free energies were computed at the PCM-ωB97X-D/def2-TZVP//PCM-B97-D/def2-TZVP level of theory.[110, 154, 192, 196] This level of theory, which accounts for the sundry dispersion-driven non-covalent interactions operative in these transition states, predicts *ee*'s that are in excellent agreement with experimental enantioselectivities. Atomic charges were computed using natural population analysis.[60] Throughout, cyclohexene oxide was used as a representative epoxide and thiophenol was used as a representative nucleophile (except where noted). All computations were performed using Gaussian 09[119] and the B97-D computations employed density fitting techniques. Images for molecular structures were generated using CYLview.[120]

CHAPTER 5

MECHANISTIC STUDIES INVESTIGATING THE ROLE OF HEXAFLUOROISOPROPANOL AND ADDITIVES IN META C-H FUNCTIONALIZATION OF ARENES[d]

---

[d] Mallojjala S. C. *et al.* To be submitted to *J. Am. Chem. Soc*.

Abstract

Directing group assisted palladium catalyzed C-H functionalization reactions are used extensively to do site-selective substitutions on arenes. Typically, these reactions use silver salts as co-catalysts to enhance the rate of the reaction. Houk and coworkers[79] demonstrated that the low-lying pathways for these reactions often involve either Pd-Ag or Pd-Pd complexes as the active catalysts. Moreover, recent experimental studies by Maiti and coworkers[80] noted that hexafluoroisopropanol (HFIP), a commonly used solvent for C-H functionalization reactions, is often vital for reactivity. There are no reports of computational studies on these reactions that address both the active catalyst responsible for the selectivity and the role of HFIP simultaneously. Herein, we report computational studies on a *meta-selective* C-H alkylation reaction catalyzed by palladium acetate to understand the role played by HFIP and to identify the active catalysts. The active pathway for the *meta* product was found to proceed via a Pd-glycine intermediate with participation of two HFIP molecules and with the 1,2-migratory insertion as the turnover determining step. The inclusion of explicit HFIP molecules lowered the enthalpy barrier by 13 kcal/mol, revealing its vital role in these reactions.

Introduction

Functionalizing inert C-H bonds has been of great interest owing to the potential of synthesizing complex organic molecules with far reaching applications.[78, 197] Many earlier efforts focused on *ortho*-functionalization of arenes by strategically installing directing groups on the arene.[78, 198-200] However, such a directing group based approach was found to be lacking for the *meta* and *para* functionalization of arenes. Recently, Yu,[201] and Maiti[80, 201-204] have employed nitrile and pyrimidine groups as directing groups attached to a linker to facilitate distal *meta*/*para* functionalization. This strategy heavily relies on the conformational flexibility of the linker employed and Maiti and coworkers[80] have reported examples of distal C-H functionalization for different linker lengths thereby demonstrating the tunability of this strategy.

Palladium salts remain the choice of catalysts among other transition metal salts owing to their functional group tolerance.[205] The use of additives such as silver carbonate, silver acetate, and cesium fluoride has increasingly gained prominence since a seminal report by Mori and coworkers[206] in 2004 using silver fluoride as a co-catalyst along with Pd(II) for an oxidative dimerization reaction. However, the first X-ray crystallographic evidence for a palladium-silver bimetallic system was reported by Hor *et al*.[207] A computational investigation of distal *meta* C-H activation with a nitrile template by Wu, Yu, Houk and coworkers[79] further shed light on the role played by bimetallic complexes in C-H activation reactions. They identified C-H activation step catalyzed by $[PdAg(\mu\text{-}OAc)_3]$ as the lowest-lying pathway. Furthermore, they identified the monometallic catalyzed C-H activation pathway to be disfavored by 12 kcal/mol. Further studies by Sunoj, Schaefer and coworkers[54, 208] identified the stabilizing interactions of

[PdAg(μ-OAc)3] on the transition states (TSs) leading to the major product in the C-H activation step. Together these studies have highlighted the importance of investigating the role played by additives in mechanistic studies of Pd-catalyzed C-H activation reactions.

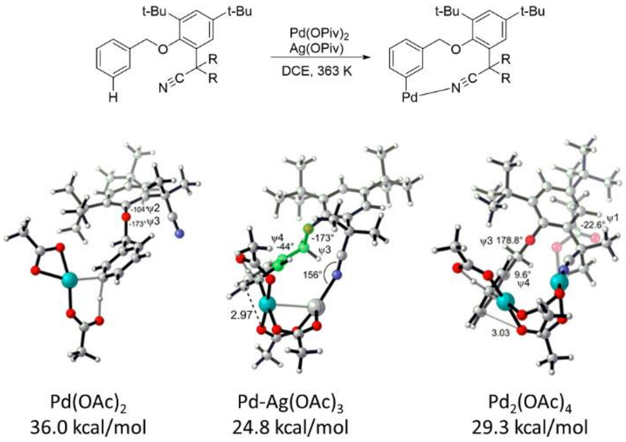

Pd(OAc)$_2$
36.0 kcal/mol

Pd-Ag(OAc)$_3$
24.8 kcal/mol

Pd$_2$(OAc)$_4$
29.3 kcal/mol

Figure 14 *meta*-C-H activation reaction investigated by Houk and coworkers.[79] [Figure adapted with permission of the journal, *J. Am. Chem. Soc.*, **2014**, 136, 1, 344-355]

Furthermore, numerous palladium catalyzed distal C-H activation reactions have used hexafluoroisopropanol (HFIP) as a preferred solvent.[81] HFIP is a polar protic solvent and is a hydrogen bond donor and an acceptor due to the presence of an alcohol group and six fluorine atoms. Due to this, it has been traditionally employed as a choice of solvent for activating carbonyls and epoxides.[82] Liu and Maiti[55] exploited the hydrogen bonding ability of HFIP in a *para* selective nitrile directed distal silylation reaction catalyzed by Pd(II). Computational studies and NMR experiments revealed strong hydrogen bonding interactions with the ether linker as the key factor for the observed selectivity. Despite this, there is still a gap in our understanding of the role played by HFIP in pyrimidine directed distal functionalization. Furthermore, there are no computational studies exploring the role played by HFIP in bimetallic pathways. Herein, we report computational studies of a pyrimidine directed distal C-H allylation reaction reported by Maiti and coworkers.[80]

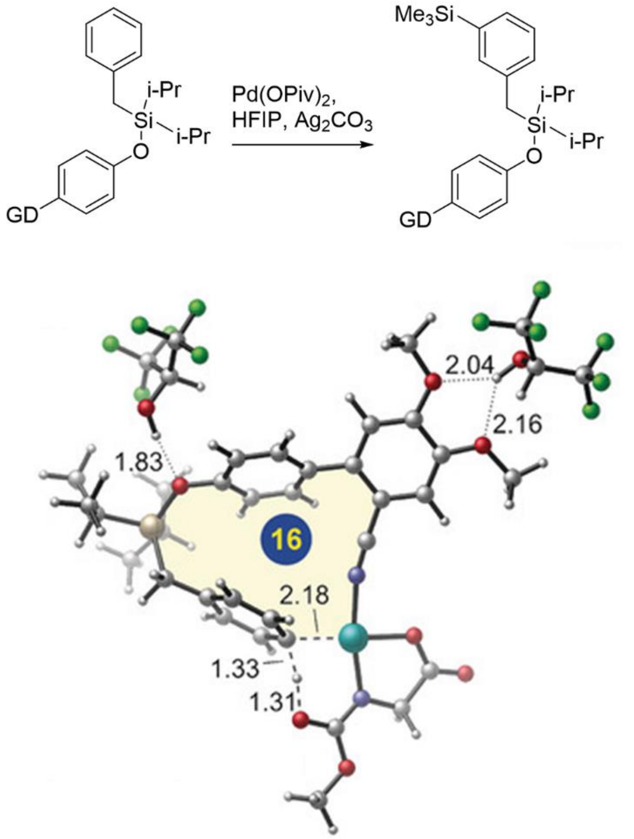

Figure 15 Maiti and Liu's[55] hydrogen-bond promoted silylation reaction demonstrating the stabilizing effects of HFIP. [Figure adapted with permission of the journal, *Angew. Chem. Int. Ed.*, **2017**, 56, 47, 14903-14907]

Results and Discussion

A Pd-catalyzed *meta* C-H alkylation reaction reported by Maiti *et al*.[80] (Scheme 11) was chosen as a model reaction to investigate the mechanistic role played by HFIP. Silver acetate was used as an oxidant for this reaction. C-H activation with mononuclear palladium acetate as the active catalyst can proceed via four different pathways, *viz.* oxidative addition, electrophilic aromatic substitution, concerted metalationdeprotonation, and σ-bond metathesis. Houk and coworkers[79] examined all four pathways and reported the concerted metallation-deprotonation pathway as the most favorable pathway for palladium catalyzed C-H activation reactions. The mechanism for the monomeric palladium acetate pathway without HFIP is shown in Scheme 12. First, palladium acetate coordinates with pyrimidine and activates the arene carbon, eliminating a molecule of acetic acid. In the second step, the allyl alcohol first forms a complex with palladium, followed by a 1,2-migratory insertion. Finally, palladium can abstract one of the two available β-hydrogen atoms via a β-hydride elimination pathway.

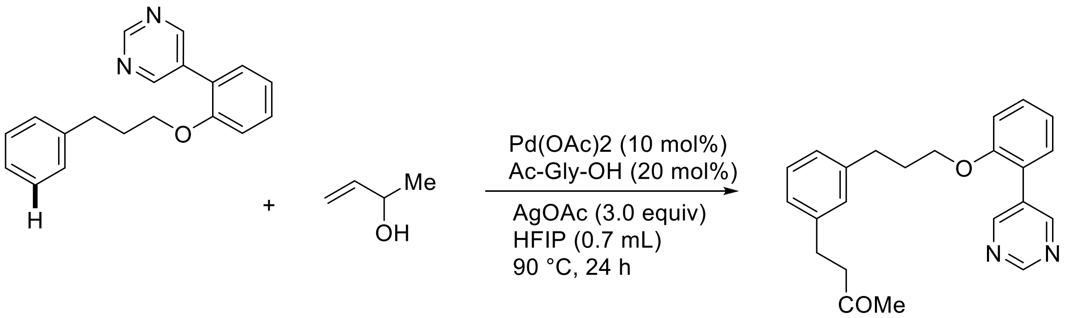

Scheme 11 Pyrimidine directed distal arene *meta*-alkylation reaction reported by Maiti and coworkers. [80]

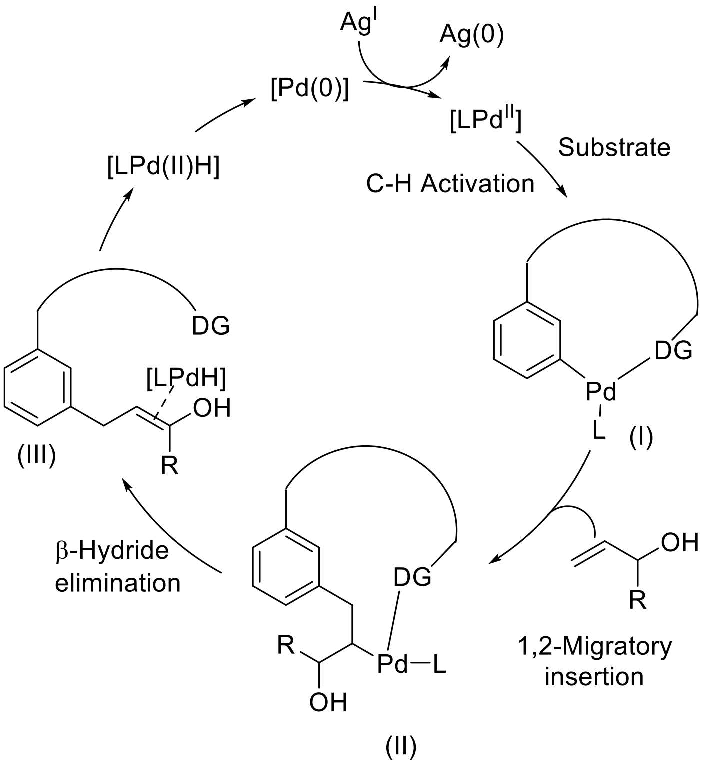

Scheme 12 Catalytic cycle for monomeric palladium acetate pathway. Pyrimidine directing group is represented by DG.

We identified six potential active catalytic species present in the solution (Scheme 13). TS optimizations were performed for *ortho*-, *meta*-, *para*- C-H activation and migratory insertion for all the potentially active catalytic species with no explicit HFIP molecules, one HFIP molecule and two HFIP molecules. Literature reports[55, 79] on the barriers for β-hydride elimination were much smaller than those for C-H activation or migratory insertion. Consequently, we chose to model β-hydride elimination using monomeric palladium acetate without any explicit HFIP molecules to reduce the computational cost.

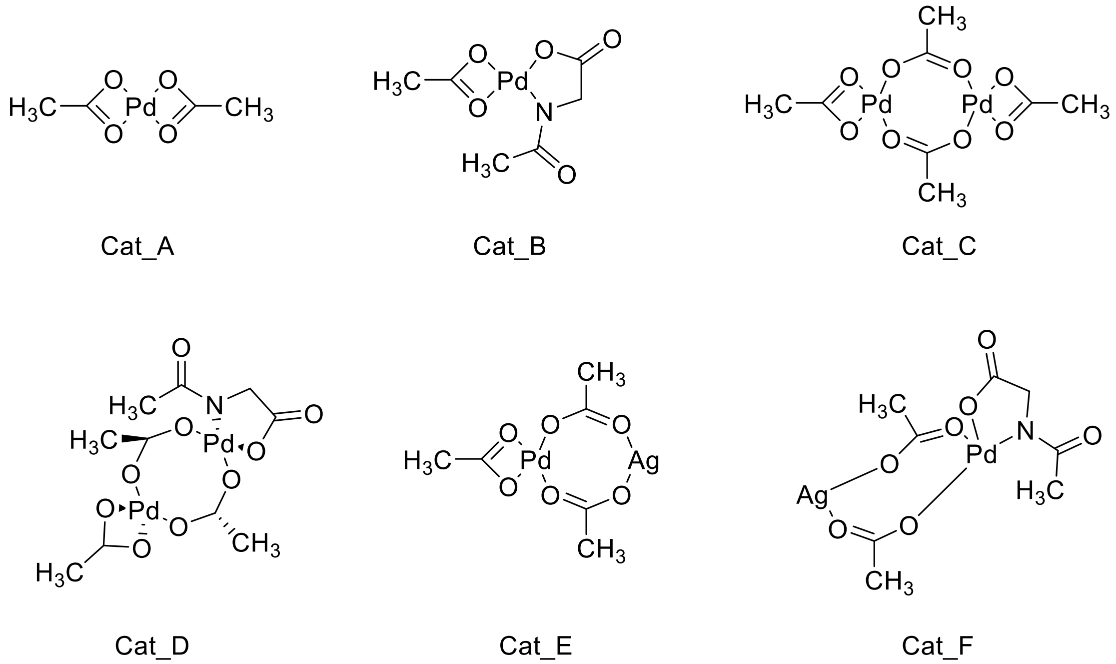

Scheme 13 Active catalytic species investigated in this study.

The active catalytic species for the lowest-lying pathway for *meta* C-H alkylation was found to involve Cat_B. The computed enthalpy barrier for the TS leading to the *meta* C-H activation ($\mathrm{TS}_{\text{m-CHCat\_B}}$) is 22.7 kcal/mol with two explicit HFIP molecules, while that for *ortho* is 23.0 kcal/mol. For *para* C-H activation, C-H activation catalyzed by Cat_E is the lowest-lying pathway with an enthalpy barrier of 21.6 kcal/mol. Table 18 in Appendix D summarizes the computed enthalpy barriers for all the catalytic species for the C-H activation step.

The turnover determining step was identified to be the 1,2-migratory insertion. The computed enthalpy barrier for the TS leading to the *meta* product ($\mathrm{TS}_{\text{m-MICat\_A}}$) was found to be 23.5 kcal/mol. This pathway proceeds most favorably in the presence of two explicit HFIP molecules but without glycine as the ligand (see Figure 14), which is consistent with previous report by Paton, Maiti and coworkers.[209] Interestingly, the computed barrier for 1,2-migratory insertion for the meta product with glycine as the ligand was found to be 1.2 kcal/mol higher than the computed barrier without glycine. Similarly, the computed barriers for *ortho* (Cat_A) and *para* (Cat_E) were found to be 30.0 and 26.9 kcal/mol respectively.

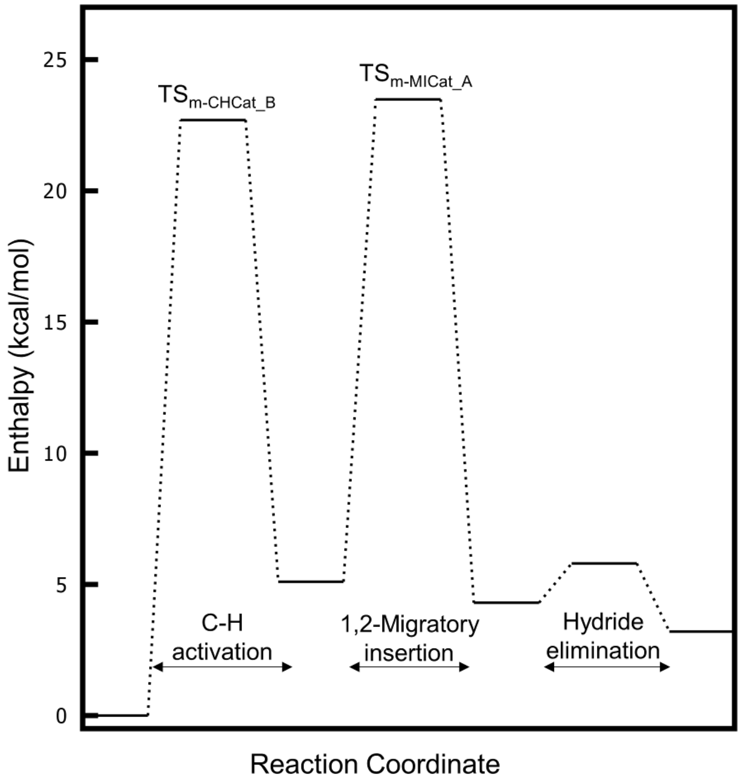

Figure 16 Potential energy surface for meta C-H alkylation reaction for the lowest-lying pathway.

Furthermore, the computed enthalpy barriers for the C-H activation step with one HFIP molecule were found to be disfavored to the lowest-lying pathway by a maximum of 9 kcal/mol, while not including any explicit HFIP molecules incurred a maximum energetic penalty of 13 kcal/mol for all the active catalysts examined. However, for the

1,2-migratory insertion, the inclusion of one explicit HFIP molecule incurred a maximum enthalpic penalty of 5 kcal/mol compared to the lowest-lying pathway, while leaving out both the HFIP molecules incurred a maximum enthalpic penalty of 8 kcal/mol. In other words, for both steps the presence of two HFIP molecules leads to substantial stabilization and rate acceleration, explaining the finding that HFIP is vital for this reaction to proceed. This stabilizing effects can be attributed to numerous CH···F interactions between the HFIP molecules and the directing group along with strong OH···O and NH···O hydrogen bonding interactions (see Figure 14).

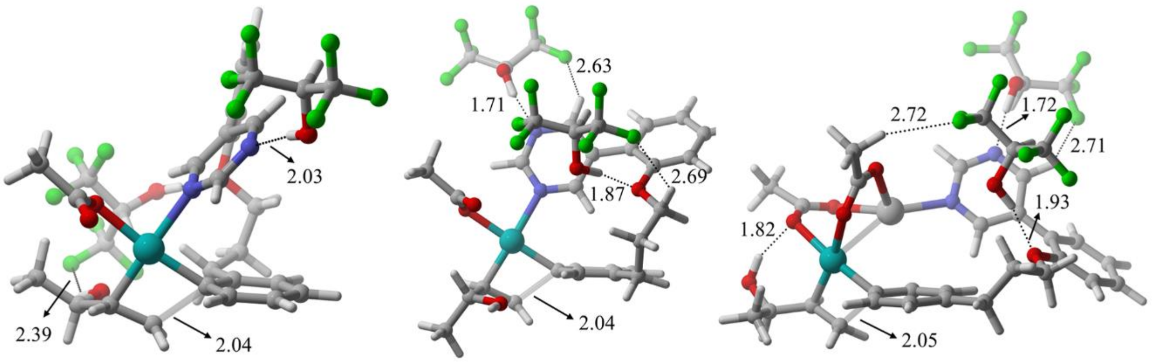

$TS_{o\text{-}MICat\_A}$ (30.0 kcal/mol) $TS_{m\text{-}MICat\_A}$ (23.5 kcal/mol) $TS_{p\text{-}MICat\_E}$ (26.9 kcal/mol)

Figure 17 Lowest-lying TS geometries for the turnover determining step (enthalpy barriers in parenthesis).

Our computed enthalpy barrier for the direct β-hydride elimination of the proton next to the oxygen was found to be 8.8 kcal/mol. However, no explicit HFIP molecules were included while computing this barrier and hence the barrier for β-hydride elimination is likely lower than this computed value. The computed selectivity (98%) with 1,2-migratory insertion as the turnover determining step was found to be in excellent agreement with the experimental value (95%; *m*:others= 20:1). Furthermore, we found additional competing pathways for *meta-selective* C-H activation and 1,2-migratory insertion catalyzed by Cat_E with an enthalpy barrier of 22.1 kcal/mol and 26.5 kcal/mol respectively (Table 18 and Table 19 Appendix D).

Conclusions

We reported a detailed computational study on a *meta-selective* pyrimidine group directed distal C-H activation reaction to investigate the role of additives and HFIP in the mechanism and to identify the active catalytic species. Migratory insertion was identified as the turnover determining step. Two distinct mechanisms were found to be in action. For *meta* and *ortho*, palladium was found to coordinate with the glycine for the C-H activation step, while for *para*, a palladium silver acetate complex is the active catalytic species. We found that HFIP forms hydrogen bonds with the non coordinating nitrogen of the pyrimidine directing group and the ether linker. We also identified stabilizing sp^2 C-H···F interactions in all the transition states. The net result of the inclusion of two HFIP molecules is substantial stabilization of the key transition states, explaining the experimental observation that HFIP is vital for this transformation. While HFIP is not always vital for related reactions, it is commonly found to provide enhanced rates, suggesting that HFIP provides similar stabilization of rate limiting TS structures in other C-H activation reactions.

Computational Methods

Density functional theory was employed for geometry optimizations, identifying transition states, and computing vibrational frequencies using Gaussian 09.[119] The

B3LYP/def2-SVP level of theory[152, 210] was employed for transition state optimization, computing vibrational frequencies and enthalpy corrections. wB97X-D/def2-tzvp[110, 114] was employed for single point computations and natural population analysis.[60] All the transition states were verified by the presence of one imaginary vibrational mode. A thorough conformational search was performed by scanning around key dihedral angles. Enthalpy corrections were based on the quasi-rigid rotor harmonic oscillator (Quasi-RRHO) approximation of Grimme.[194] Solvent effects were accounted for by employing the SMD solvent model and by including explicit solvent molecules wherever noted. Due to the unavailability of cavity parameters for hexafluoroisopropanol in Gaussian09, isopropanol was used for defining the cavity along with the dielectric constant of hexafluoroisopropanol as reported by Liu, Maiti and coworkers.[55] Images for molecular structures were generated using CYLview.[120]

CHAPTER 6

CONCLUSIONS

Through these four studies, I have applied modern computational methods and techniques to elucidate the structure, reactivity and mechanism of complex organic systems. First, I studied various aza-thia cryptands and elucidated the structures of the lowest-lying conformations. I identified cryptands capable of chelating Cu(I) and (II) ions. For my second study, I solved the ground state structure of [18]annulene and resolve the discrepancy between past computational and experimental efforts. Furthermore, I established the mechanism of inner/outer proton interconversion in [18]annulene to explain the coalescence observed in NMR chemical shifts at elevated temperatures. In my third study, I identified strong electrostatic perturbations in the chiral pocket caused by alkali metal ions in chiral alkali metal phosphates as the primary reason for the observed stereo reversal compared to a chiral phosphoric acid. For my final study, I established the need for including explicit hexafluoroisopropanol molecules in computational mechanistic studies of palladium catalyzed C-H functionalization reaction the importance of investigating the bimetallic Ag-Pd and Pd-Pd complex catalyzed pathways for C-H functionalization reaction. Together, these four projects demonstrate the importance of modern computational investigations in structure elucidation and mechanistic exploration.

REFERENCES

1. Fernandez, I.; Cossio, F. P., Applied computational chemistry. *Chem Soc Rev* **2014,** *43* (14), 4906.

2. Houk, K. N., Foreword: applied computational chemistry. *Chem Soc Rev* **2014,** *43* (14), 4905.

3. Kronik, L.; Tkatchenko, A., Understanding molecular crystals with dispersion-inclusive density functional theory: pairwise corrections and beyond. *Acc Chem Res* **2014,** *47* (11), 3208.

4. Bredas, J. L.; Houk, K. N., DFT elucidation of materials properties. *Acc Chem Res* **2014,** *47* (11), 3207.

5. Frenking, G.; Tonner, R.; Klein, S.; Takagi, N.; Shimizu, T.; Krapp, A.; Pandey, K. K.; Parameswaran, P., New bonding modes of carbon and heavier group 14 atoms Si-Pb. *Chem Soc Rev* **2014,** *43* (14), 5106.

6. Garcia-Borras, M.; Osuna, S.; Luis, J. M.; Swart, M.; Sola, M., The role of aromaticity in determining the molecular structure and reactivity of (endohedral metallo)fullerenes. *Chem Soc Rev* **2014,** *43* (14), 5089.

7. Johnson, L. E.; Dalton, L. R.; Robinson, B. H., Optimizing calculations of electronic excitations and relative hyperpolarizabilities of electrooptic chromophores. *Acc Chem Res* **2014,** *47* (11), 3258.

8. Lodewyk, M. W.; Siebert, M. R.; Tantillo, D. J., Computational prediction of 1H and 13C chemical shifts: a useful tool for natural product, mechanistic, and synthetic organic chemistry. *Chem Rev* **2012,** *112* (3), 1839.

9. Schindler, M., Magnetic-Properties in Terms of Localized Quantities .5. Carbocations. *J Am Chem Soc* **1987,** *109* (4), 1020.

10. Parthey, M.; Kaupp, M., Quantum-chemical insights into mixed-valence systems: within and beyond the Robin-Day scheme. *Chem Soc Rev* **2014,** *43* (14), 5067.

11. Cheng, G. J.; Zhang, X.; Chung, L. W.; Xu, L.; Wu, Y. D., Computational organic chemistry: bridging theory and experiment in establishing the mechanisms of chemical reactions. *J Am Chem Soc* **2015,** *137* (5), 1706.

12. Musaev, D. G.; Figg, T. M.; Kaledin, A. L., Versatile reactivity of Pd-catalysts: mechanistic features of the mono-N-protected amino acid ligand and cesium-halide base in Pd-catalyzed C-H bond functionalization. *Chem Soc Rev* **2014,** *43* (14), 5009.

13. Usharani, D.; Lai, W.; Li, C.; Chen, H.; Danovich, D.; Shaik, S., A tutorial for understanding chemical reactivity through the valence bond approach. *Chem Soc Rev* **2014,** *43* (14), 4968.

14. Bowen, J. P.; Allinger, N. L., Molecular Mechanics: The Art and Science of Parameterization. *Rev Comput Chem* **1991**, 81.

15. Lam, Y. H.; Grayson, M. N.; Holland, M. C.; Simon, A.; Houk, K. N., Theory and Modeling of Asymmetric Catalytic Reactions. *Acc Chem Res* **2016,** *49* (4), 750.

16. Hansen, E.; Rosales, A. R.; Tutkowski, B.; Norrby, P. O.; Wiest, O., Prediction of Stereochemistry using Q2MM. *Acc Chem Res* **2016,** *49* (5), 996.

17. Grimme, S., Accurate description of van der Waals complexes by density functional theory including empirical corrections. *J Comput Chem* **2004,** *25* (12), 1463.

18. Balcells, D.; Clot, E.; Eisenstein, O.; Nova, A.; Perrin, L., Deciphering Selectivity in Organic Reactions: A Multifaceted Problem. *Acc Chem Res* **2016,** *49* (5), 1070.

19. Maji, R.; Mallojjala, S. C.; Wheeler, S. E., Chiral phosphoric acid catalysis: from numbers to insights. *Chem Soc Rev* **2018,** *47* (4), 1142.

20. Park, Y.; Ahn, S.; Kang, D.; Baik, M. H., Mechanism of Rh-Catalyzed Oxidative Cyclizations: Closed versus Open Shell Pathways. *Acc Chem Res* **2016,** *49* (6), 1263.

21. Peng, Q.; Duarte, F.; Paton, R. S., Computing organic stereoselectivity - from concepts to quantitative calculations and predictions. *Chem Soc Rev* **2016,** *45* (22), 6093.

22. Peng, Q.; Paton, R. S., Catalytic Control in Cyclizations: From Computational Mechanistic Understanding to Selectivity Prediction. *Acc Chem Res* **2016,** *49* (5), 1042.

23. Reid, J. P.; Simon, L.; Goodman, J. M., A Practical Guide for Predicting the Stereochemistry of Bifunctional Phosphoric Acid Catalyzed Reactions of Imines. *Acc Chem Res* **2016,** *49* (5), 1029.

24. Santoro, S.; Kalek, M.; Huang, G.; Himo, F., Elucidation of Mechanisms and Selectivities of Metal-Catalyzed Reactions using Quantum Chemical Methodology. *Acc Chem Res* **2016,** *49* (5), 1006.

25. Sperger, T.; Sanhueza, I. A.; Schoenebeck, F., Computation and Experiment: A Powerful Combination to Understand and Predict Reactivities. *Acc Chem Res* **2016,** *49* (6), 1311.

26. Sunoj, R. B., Transition State Models for Understanding the Origin of Chiral Induction in Asymmetric Catalysis. *Acc Chem Res* **2016,** *49* (5), 1019.

27. Tantillo, D. J., Faster, Catalyst! React! React! Exploiting Computational Chemistry for Catalyst Development and Design. *Acc Chem Res* **2016,** *49* (6), 1079.

28. Walden, D. M.; Ogba, O. M.; Johnston, R. C.; Cheong, P. H., Computational Insights into the Central Role of Nonbonding Interactions in Modern Covalent Organocatalysis. *Acc Chem Res* **2016,** *49* (6), 1279.

29. Wheeler, S. E.; Seguin, T. J.; Guan, Y.; Doney, A. C., Noncovalent Interactions in Organocatalysis and the Prospect of Computational Catalyst Design. *Acc Chem Res* **2016,** *49* (5), 1061.

30. Zhang, X.; Chung, L. W.; Wu, Y. D., New Mechanistic Insights on the Selectivity of Transition-Metal-Catalyzed Organic Reactions: The Role of Computational Chemistry. *Acc Chem Res* **2016,** *49* (6), 1302.

31. Bickelhaupt, F. M.; Houk, K. N., Analyzing Reaction Rates with the Distortion/Interaction-Activation Strain Model. *Angew Chem Int Ed* **2017,** *56* (34), 10070.

32. Ess, D. H.; Houk, K. N., Distortion/interaction energy control of 1,3-dipolar cycloaddition reactivity. *J Am Chem Soc* **2007,** *129* (35), 10646.

33. Fernandez, I.; Bickelhaupt, F. M., The activation strain model and molecular orbital theory: understanding and designing chemical reactions. *Chem Soc Rev* **2014,** *43* (14), 4953.

34. Morokuma, K., Molecular Orbital Studies of Hydrogen Bonds. III. C=O⋯H–O Hydrogen Bond in H2CO⋯H2O and H2CO⋯2H2O. *J Chem Phys* **1971,** *55* (3), 1236.

35. Ziegler, T.; Rauk, A., On the calculation of bonding energies by the Hartree Fock Slater method. *Theo Chim Acta* **1977,** *46* (1), 1.

36. Jeziorski, B.; Moszynski, R.; Szalewicz, K., Perturbation-Theory Approach to Intermolecular Potential-Energy Surfaces of Van-Der-Waals Complexes. *Chem Rev* **1994,** *94* (7), 1887.

37. Szalewicz, K., Symmetry-adapted perturbation theory of intermolecular forces. *Wiley Interdiscip Rev Comput Mol Sci* **2012,** *2* (2), 254.

38. Hohenstein, E. G.; Sherrill, C. D., Density fitting of intramonomer correlation effects in symmetry-adapted perturbation theory. *J Chem Phys* **2010,** *133* (1), 014101.

39. Hohenstein, E. G.; Sherrill, C. D., Density fitting and Cholesky decomposition approximations in symmetry-adapted perturbation theory: Implementation and application to probe the nature of pi-pi interactions in linear acenes. *J Chem Phys* **2010,** *132* (18), 184111.

40. Parker, T. M.; Burns, L. A.; Parrish, R. M.; Ryno, A. G.; Sherrill, C. D., Levels of symmetry adapted perturbation theory (SAPT). I. Efficiency and performance for interaction energies. *J Chem Phys* **2014,** *140* (9), 094106.

41. Johnson, E. R.; Keinan, S.; Mori-Sanchez, P.; Contreras-Garcia, J.; Cohen, A. J.; Yang, W., Revealing noncovalent interactions. *J Am Chem Soc* **2010,** *132* (18), 6498.

42. Lu, T.; Wheeler, S. E., Quantifying the role of anion-pi interactions in anion-pi catalysis. *Org Lett* **2014,** *16* (12), 3268.

43. Maji, R.; Wheeler, S. E., Importance of Electrostatic Effects in the Stereoselectivity of NHC-Catalyzed Kinetic Resolutions. *J Am Chem Soc* **2017,** *139* (36), 12441.

44. Maji, R.; Champagne, P. A.; Houk, K. N.; Wheeler, S. E., Activation Mode and Origin of Selectivity in Chiral Phosphoric Acid-Catalyzed Oxacycle Formation by Intramolecular Oxetane Desymmetrizations. *ACS Catal* **2017,** *7* (10), 7332.

45. Seguin, T. J.; Wheeler, S. E., Stacking and Electrostatic Interactions Drive the Stereoselectivity of Silylium-Ion Asymmetric Counteranion-Directed Catalysis. *Angew Chem Int Ed* **2016,** *55* (51), 15889.

46. Warshel, A.; Sharma, P. K.; Kato, M.; Xiang, Y.; Liu, H.; Olsson, M. H., Electrostatic basis for enzyme catalysis. *Chem Rev* **2006,** *106* (8), 3210.

47. Fried, S. D.; Bagchi, S.; Boxer, S. G., Extreme electric fields power catalysis in the active site of ketosteroid isomerase. *Science* **2014,** *346* (6216), 1510.

48. Wu, Y.; Boxer, S. G., A Critical Test of the Electrostatic Contribution to Catalysis with Noncanonical Amino Acids in Ketosteroid Isomerase. *J Am Chem Soc* **2016,** *138* (36), 11890.

49. Seguin, T. J.; Wheeler, S. E., Electrostatic Basis for Enantioselective Brønsted-Acid-Catalyzed Asymmetric Ring Openings of meso-Epoxides. *ACS Catal* **2016,** *6* (4), 2681.

50. Seguin, T. J.; Wheeler, S. E., Competing Noncovalent Interactions Control the Stereoselectivity of Chiral Phosphoric Acid Catalyzed Ring Openings of 3-Substituted Oxetanes. *ACS Catal* **2016,** *6* (10), 7222.

51. Seguin, T. J.; Lu, T.; Wheeler, S. E., Enantioselectivity in Catalytic Asymmetric Fischer Indolizations Hinges on the Competition of pi-Stacking and CH/pi Interactions. *Org Lett* **2015,** *17* (12), 3066.

52. Toste, F. D.; Sigman, M. S.; Miller, S. J., Pursuit of Noncovalent Interactions for Strategic Site-Selective Catalysis. *Acc Chem Res* **2017,** *50* (3), 609.

53. Neel, A. J.; Hilton, M. J.; Sigman, M. S.; Toste, F. D., Exploiting non-covalent pi interactions for catalyst design. *Nature* **2017,** *543* (7647), 637.

54. Anand, M.; Sunoj, R. B.; Schaefer, H. F., 3rd, Non-innocent additives in a palladium(II)-catalyzed C-H bond activation reaction: insights into multimetallic active catalysts. *J Am Chem Soc* **2014,** *136* (15), 5535.

55. Maji, A.; Guin, S.; Feng, S.; Dahiya, A.; Singh, V. K.; Liu, P.; Maiti, D., Experimental and Computational Exploration of para-Selective Silylation with a Hydrogen-Bonded Template. *Angew Chem Int Ed* **2017,** *56* (47), 14903.

56. Knowles, R. R.; Jacobsen, E. N., Attractive noncovalent interactions in asymmetric catalysis: links between enzymes and small molecule catalysts. *Proc Natl Acad Sci* **2010,** *107* (48), 20678.

57. Uyeda, C.; Jacobsen, E. N., Transition-state charge stabilization through multiple non-covalent interactions in the guanidinium-catalyzed enantioselective Claisen rearrangement. *J Am Chem Soc* **2011,** *133* (13), 5062.

58. Kitaura, K.; Morokuma, K., A new energy decomposition scheme for molecular interactions within the Hartree-Fock approximation. *Int J Quant Chem* **1976,** *10* (2), 325.

59. E. D. Glendening, A. E. R., J. E. Carpenter, F. Weinhold, NBO Version 3.1.

60. Reed, A. E.; Weinstock, R. B.; Weinhold, F., Natural-Population Analysis. *J Chem Phys* **1985,** *83* (2), 735.

61. Penfield, K. W.; Gewirth, A. A.; Solomon, E. I., Electronic-Structure and Bonding of the Blue Copper Site in Plastocyanin. *J Am Chem Soc* **1985,** *107* (15), 4519.

62. Farver, O.; Pecht, I., Electron transfer in blue copper proteins. *Coord Chem Rev* **2011,** *255* (7-8), 757.

63. Fontecave, M.; Pierre, J. L., Oxidations by copper metalloenzymes and some biomimetic approaches. *Coord Chem Rev* **1998,** *170* (1), 125.

64. Lehn, J. M., Cryptates: macropolycyclic inclusion complexes. *Pure and Applied Chemistry* **1977,** *49* (6), 857.

65. Wannere, C. S.; von Rague Schleyer, P., How aromatic are large (4n + 2)pi annulenes? *Org Lett* **2003,** *5* (6), 865.

66. Wannere, C. S.; Sattelmeyer, K. W.; Schaefer, H. F., 3rd; Schleyer, P., Aromaticity: the alternating C--C bond length structures of [14]-, [18]-, and [22]annulene. *Angew Chem Int Ed* **2004,** *43* (32), 4200.

67. Hudson, B. S.; Allis, D. G., The structure of [18]-annulene: Computed Raman spectra, zero-point level and proton NMR chemical shifts. *J Mol Struct* **2012,** *1023*, 212.

68. Kwan, E. E.; Liu, R. Y., Enhancing NMR Prediction for Organic Compounds Using Molecular Dynamics. *J Chem Theory Comput* **2015,** *11* (11), 5083.

69. Beezer, A. E.; Mortimer, C. T.; Springall, H. D.; Sondheimer, F.; Wolovsky, R., 33. The heat of combustion of cyclo-octadecanonaene ([18]annulene). *J Chem Soc (Resumed)* **1965,** (0), 216.

70. Oth, J. F. M.; Bünzli, J.-C.; de Julien de Zélicourt, Y., The Stabilization Energy of [18] Annulene. A thermochemical determination. *Helv Chim Acta* **1974,** *57* (7), 2276.

71. Oth, J. F. M., Conformational mobility and fast bond shift in the annulenes. In *Pure Appl Chem*, 1971; Vol. 25, p 573.

72. Parmar, D.; Sugiono, E.; Raja, S.; Rueping, M., Complete field guide to asymmetric BINOL-phosphate derived Bronsted acid and metal catalysis: history and classification by mode of activation; Bronsted acidity, hydrogen bonding, ion pairing, and metal phosphates. *Chem Rev* **2014,** *114* (18), 9047.

73. Parmar, D.; Sugiono, E.; Raja, S.; Rueping, M., Addition and Correction to Complete Field Guide to Asymmetric BINOL-Phosphate Derived Bronsted Acid and Metal Catalysis: History and Classification by Mode of Activation; Bronsted Acidity, Hydrogen Bonding, Ion Pairing, and Metal Phosphates. *Chem Rev* **2017,** *117* (15), 10608.

74. Rueping, M.; Theissmann, T.; Kuenkel, A.; Koenigs, R. M., Highly enantioselective organocatalytic carbonyl-ene reaction with strongly acidic, chiral Bronsted acids as efficient catalysts. *Angew Chem Int Ed* **2008,** *47* (36), 6798.

75. Xu, S.; Wang, Z.; Zhang, X.; Zhang, X.; Ding, K., Chiral Bronsted acid catalyzed asymmetric Baeyer-Villiger reaction of 3-substituted cyclobutanones by using aqueous H2O2. *Angew Chem Int Ed* **2008,** *47* (15), 2840.

76. Hatano, M.; Moriyama, K.; Maki, T.; Ishihara, K., Which is the actual catalyst: chiral phosphoric Acid or chiral calcium phosphate? *Angew Chem Int Ed* **2010,** *49* (22), 3823.

77. Ingle, G.; Mormino, M. G.; Antilla, J. C., Lithium BINOL phosphate catalyzed desymmetrization of meso-epoxides with aromatic thiols. *Org Lett* **2014,** *16* (21), 5548.

78. Sambiagio, C.; Schonbauer, D.; Blieck, R.; Dao-Huy, T.; Pototschnig, G.; Schaaf, P.; Wiesinger, T.; Zia, M. F.; Wencel-Delord, J.; Besset, T.; Maes, B. U. W.; Schnurch, M., A comprehensive overview of directing groups applied in metal-catalysed C-H functionalisation chemistry. *Chem Soc Rev* **2018,** *47* (17), 6603.

79. Yang, Y. F.; Cheng, G. J.; Liu, P.; Leow, D.; Sun, T. Y.; Chen, P.; Zhang, X.; Yu, J. Q.; Wu, Y. D.; Houk, K. N., Palladium-catalyzed meta-selective C-H bond activation with a nitrile-containing template: computational study on mechanism and origins of selectivity. *J Am Chem Soc* **2014,** *136* (1), 344.

80. Jayarajan, R.; Das, J.; Bag, S.; Chowdhury, R.; Maiti, D., Diverse meta-C-H Functionalization of Arenes across Different Linker Lengths. *Angew Chem Int Ed* **2018,** *57* (26), 7659.

81. Sinha, S. K.; Bhattacharya, T.; Maiti, D., Role of hexafluoroisopropanol in C–H activation. *React Chem Eng* **2019,** *4* (2), 244.

82. Colomer, I.; Chamberlain, A. E. R.; Haughey, M. B.; Donohoe, T. J., Hexafluoroisopropanol as a highly versatile solvent. *Nature Reviews Chemistry* **2017,** *1* (11).

83. Pedersen, C. J., Cyclic polyethers and their complexes with metal salts. *J Am Chem Soc* **1967,** *89* (26), 7017.

84. Pedersen, C. J., Cyclic polyethers and their complexes with metal salts. *Journal of the American Chemical Society* **1967,** *89* (10), 2495.

85. Dietrich, B.; Lehn, J. M.; Sauvage, J. P., Diaza-polyoxa-macrocycles et macrobicycles. *Tetrahedron Letters* **1969,** *10* (34), 2885.

86. Cram, D. J.; Cram, J. M., Host-Guest Chemistry. *Science* **1974,** *183* (4127), 803.

87. Cram, D. J.; Kaneda, T.; Helgeson, R. C.; Lein, G. M., Spherands - ligands whose binding of cations relieves enforced electron-electron repulsions. *Journal of the American Chemical Society* **1979,** *101* (22), 6752.

88. Kyba, E. P.; Helgeson, R. C.; Madan, K.; Gokel, G. W.; Tarnowski, T. L.; Moore, S. S.; Cram, D. J., Host-guest complexation. 1. Concept and illustration. *Journal of the American Chemical Society* **1977,** *99* (8), 2564.

89. Alibrandi, G.; Amendola, V.; Bergamaschi, G.; Fabbrizzi, L.; Licchelli, M., Bistren cryptands and cryptates: versatile receptors for anion inclusion and recognition in water. *Organic & Biomolecular Chemistry* **2015,** *13* (12), 3510.

90. Dye, J. L.; Andrews, C. W.; Mathews, S. E., Strategies for the preparation of compounds of alkali metal anions. *The Journal of Physical Chemistry* **1975,** *79* (26), 3065.

91. Paul, P.; Nag, K., Sulfur-nitrogen-bonded metal chelates. 16. Reactivities of coordinated nitriles in the nickel(II) complexes [Ni(SNN)(NCR)](ClO4) with alcohols, amines, and different nucleophiles. Synthesis, characterization, and stereochemistry of imino-ether, amide, and amidine complexes. *Inorganic Chemistry* **1987,** *26* (10), 1586.

92. Cangelosi, V. M.; Carter, T. G.; Crossland, J. L.; Zakharov, L. N.; Johnson, D. W., Self-Assembled E2L3 Cryptands (E = P, As, Sb, Bi): Transmetalation, Homo- and Heterometallic Assemblies, and Conformational Isomerism. *Inorganic Chemistry* **2010,** *49* (21), 9985.

93. Evans, N. H.; Beer, P. D., Advances in Anion Supramolecular Chemistry: From Recognition to Chemical Applications. *Angewandte Chemie International Edition* **2014,** *53* (44), 11716.

94. Sarkar, B.; Mukhopadhyay, P.; Bharadwaj, P. K., Laterally non-symmetric aza-cryptands: synthesis, catalysis and derivatization to new receptors. *Coordination Chemistry Reviews* **2003,** *236* (1-2), 1.

95. Vasdev, N.; Cao, P.; van Oosten, E. M.; Wilson, A. A.; Houle, S.; Hao, G.; Sun, X.; Slavine, N.; Alhasan, M.; Antich, P. P.; Bonte, F. J.; Kulkarni, P., Synthesis and PET imaging studies of [18F]2-fluoroquinolin-8-ol ([18F]CABS13) in transgenic mouse models of Alzheimer's disease. *MedChemComm* **2012,** *3* (10), 1228.

96. Anderson, C. J.; Wadas, T. J.; Wong, E. H.; Weisman, G. R., Cross-bridged macrocyclic chelators for stable complexation of copper radionuclides for PET imaging. *The quarterly journal of nuclear medicine and molecular imaging : official publication of the Italian Association of Nuclear Medicine (AIMN) [and] the International Association of Radiopharmacology (IAR), [and] Section of the Society of...* **2008,** *52* (2), 185.

97. Sprague, J. E.; Peng, Y.; Sun, X.; Weisman, G. R.; Wong, E. H.; Achilefu, S.; Anderson, C. J., Preparation and biological evaluation of copper-64-labeled tyr3-octreotate using a cross-bridged macrocyclic chelator. *Clin Cancer Res* **2004,** *10* (24), 8674.

98. Wong, E. H.; Weisman, G. R.; Hill, D. C.; Reed, D. P.; Rogers, M. E.; Condon, J. S.; Fagan, M. A.; Calabrese, J. C.; Lam, K.-C.; Guzei, I. A.; Rheingold, A. L., Synthesis and Characterization of Cross-Bridged Cyclams and Pendant-Armed Derivatives and Structural Studies of Their Copper(II) Complexes. *Journal of the American Chemical Society* **2000,** *122* (43), 10561.

99. Thompson, M. C.; Busch, D. H., Reactions of Coördinated Ligands. II. Nickel(II) Complexes of Some Novel Tetradentate Ligands. *Journal of the American Chemical Society* **1962,** *84* (9), 1762.

100. Thompson, M. C.; Busch, D. H., Reactions of Coordinated Ligands. IX. Utilization of the Template Hypothesis to Synthesize Macrocyclic Ligandsin Situ. *Journal of the American Chemical Society* **1964,** *86* (18), 3651.

101. Corfield, P. W. R.; Ceccarelli, C.; Glick, M. D.; Moy, I. W. Y.; Ochrymowycz, L. A.; Rorabacher, D. B., Structures of a labile copper redox couple: sterically constrained copper(II) and copper(I) complexes formed with a simple cyclic pentathia ether, 1,4,7,10,13-pentathiacyclopentadecane. *Journal of the American Chemical Society* **1985,** *107* (8), 2399.

102. Ambundo, E. A.; Ochrymowycz, L. A.; Rorabacher, D. B., Electron-transfer kinetics of tris(2-(methylthioethyl))aminecopper(II/I). A tripodal ligand complex exhibiting virtual C3v symmetry. *Inorg Chem* **2001,** *40* (20), 5133.

103. Galijasevic, S.; Krylova, K.; Koenigbauer, M. J.; Jaeger, G. S.; Bushendorf, J. D.; Heeg, M. J.; Ochrymowycz, L. A.; Taschner, M. J.; Rorabacher, D. B., Chelate ring sequence effects on thermodynamic, kinetic and electron-transfer properties of copper(ii/i) systems involving macrocyclic ligands with S4 and NS3 donor setsElectronic supplementary information (ESI) available: Tables S1–14: tabulations of experimental rate constants. See http://www.rsc.org/suppdata/dt/b3/b300602f. *Dalton Transactions* **2003,** (8), 1577.

104. Krylova, K.; Kulatilleke, C. P.; Heeg, M. J.; Salhi, C. A.; Ochrymowycz, L. A.; Rorabacher, D. B., A Structural Strategy for Generating Rapid Electron-Transfer Kinetics in Copper(II/I) Systems. *Inorganic Chemistry* **1999,** *38* (19), 4322.

105. Bernardo, M. M.; Heeg, M. J.; Schroeder, R. R.; Ochrymowycz, L. A.; Rorabacher, D. B., Comparison of the influence of saturated nitrogen and sulfur donor

atoms on the properties of copper(II/I)-macrocyclic polyamino polythiaether ligand complexes: redox potentials and protonation and stability constants of CuIL species and new structural data. *Inorganic Chemistry* **1992,** *31* (2), 191.

106. Jones, T. E.; Rorabacher, D. B., Letter: Simple models for "blue" copper proteins. The copper-thiaether complexes. *J Am Chem Soc* **1975,** *97* (26), 7485.

107. Kim, S.; Minier, M. A.; Loas, A.; Becker, S.; Wang, F.; Lippard, S. J., Achieving Reversible Sensing of Nitroxyl by Tuning the Ligand Environment of Azamacrocyclic Copper(II) Complexes. *J Am Chem Soc* **2016,** *138* (6), 1804.

108. Walker, T. L.; Taschner, I. S.; Chandra, M. S.; Taschner, M. J.; Engle, J. T.; Schrage, B. R.; Ziegler, C. J.; Gao, X.; Wheeler, S. E., Lone-Pair-Induced Topicity Observed in Macrobicyclic Tetra-thia Lactams and Cryptands: Synthesis, Spectral Identification, and Computational Assessment. *J Org Chem* **2018,** *83* (17), 10025.

109. Wheeler, S. E., Local nature of substituent effects in stacking interactions. *J Am Chem Soc* **2011,** *133* (26), 10262.

110. Weigend, F.; Ahlrichs, R., Balanced basis sets of split valence, triple zeta valence and quadruple zeta valence quality for H to Rn: Design and assessment of accuracy. *Phys Chem Chem Phys* **2005,** *7* (18), 3297.

111. Miertus, S.; Scrocco, E.; Tomasi, J., Electrostatic Interaction of a Solute with a Continuum - a Direct Utilization of Abinitio Molecular Potentials for the Prevision of Solvent Effects. *Chem Phys* **1981,** *55* (1), 117.

112. Tomasi, J.; Mennucci, B.; Cammi, R., Quantum mechanical continuum solvation models. *Chem Rev* **2005,** *105* (8), 2999.

113. Grimme, S., Supramolecular binding thermodynamics by dispersion-corrected density functional theory. *Chemistry* **2012,** *18* (32), 9955.

114. Chai, J. D.; Head-Gordon, M., Long-range corrected hybrid density functionals with damped atom-atom dispersion corrections. *Phys Chem Chem Phys* **2008,** *10* (44), 6615.

115. Adamo, C.; Barone, V., Exchange functionals with improved long-range behavior and adiabatic connection methods without adjustable parameters: The mPW and mPW1PW models. *The Journal of Chemical Physics* **1998,** *108* (2), 664.

116. Zhao, Y.; Tishchenko, O.; Truhlar, D. G., How well can density functional methods describe hydrogen bonds to pi acceptors? *J Phys Chem B* **2005,** *109* (41), 19046.

117. Hehre, W. J.; Stewart, R. F.; Pople, J. A., Self-Consistent Molecular-Orbital Methods. I. Use of Gaussian Expansions of Slater-Type Atomic Orbitals. *J Chem Phys* **1969,** *51* (6), 2657.

118. Wolinski, K.; Hinton, J. F.; Pulay, P., Efficient implementation of the gauge-independent atomic orbital method for NMR chemical shift calculations. *Journal of the American Chemical Society* **1990,** *112* (23), 8251.

119. Frisch, M.; Trucks, G.; Schlegel, H.; Scuseria, G.; Robb, M.; Cheeseman, J.; Scalmani, G.; Barone, V.; Mennucci, B.; Petersson, G.; Nakatsuji, H.; Caricato, M.; Li, X.; Hratchian, H.; Izmaylov, A.; Bloino, J.; Zheng, G.; Sonnenberg, J.; Hada, M.; Ehara, M.; Toyota, K.; Fukuda, R.; Hasegawa, J.; Ishida, M.; Nakajima, T.; Honda, Y.; Kitao, O.; Nakai, H.; Vreven, T.; Montgomery, J., JA; Peralta, J.; Ogliaro, F.; Bearpark, M.; Heyd, J.; Brothers, E.; Kudin, K.; Staroverov, V.; Keith, T.; Kobayashi, R.; Normand, J.; Raghavachari, K.; Rendell, A.; Burant, J.; Iyengar, S.; Tomasi, J.; Cossi, M.; Rega, N.;

Millam, J.; Klene, M.; Knox, J.; Cross, J.; Bakken, V.; Adamo, C.; ramillo, J.; Gomperts, R.; Stratmann, R.; Yazyev, O.; Austin, A.; Cammi, R.; Pomelli, C.; Ochterski, J.; Martin, R.; Morokuma, K.; Zakrzewski, V.; Voth, G.; Salvador, P.; Dannenberg, J.; Dapprich, S.; Daniels, A.; Farkas, O.; Foresman, J.; Ortiz, J.; Cioslowski, J.; Fox, D. *Gaussian 09, Revision D.01*, Gaussian, Inc.: 2009.

120. Legault, C. Y. *CYLview, 1.0b; Université de Sherbrooke, 2009 (http://www.cylview.org).*

121. Spitler, E. L.; Ii, C. A.; Haley, M. M., Renaissance of annulene chemistry. *Chem Rev* **2006,** *106* (12), 5344.

122. Wiberg, K. B., Antiaromaticity in monocyclic conjugated carbon rings. *Chem Rev* **2001,** *101* (5), 1317.

123. Castro, C.; Isborn, C. M.; Karney, W. L.; Mauksch, M.; von Rague Schleyer, P., Aromaticity with a twist: Mobius [4n]annulenes. *Org Lett* **2002,** *4* (20), 3431.

124. Castro, C.; Karney, W. L., Mechanisms and Möbius strips: understanding dynamic processes in annulenes. *J Phys Org Chem* **2012,** *25* (8), 612.

125. Castro, C.; Karney, W. L.; Valencia, M. A.; Vu, C. M.; Pemberton, R. P., Mobius aromaticity in [12]annulene: cis-trans isomerization via twist-coupled bond shifting. *J Am Chem Soc* **2005,** *127* (27), 9704.

126. Santander, M. V.; Pastor, M. B.; Nelson, J. N.; Castro, C.; Karney, W. L., Huckel and Mobius bond-shifting routes to configuration change in dehydro[4n+2]annulenes. *J Org Chem* **2013,** *78* (5), 2033.

127. Michel, C. S.; Lampkin, P. P.; Shezaf, J. Z.; Moll, J. F.; Castro, C.; Karney, W. L., Tunneling by 16 Carbons: Planar Bond Shifting in [16]Annulene. *J Am Chem Soc* **2019,** *141* (13), 5286.

128. Rzepa, H. S., A double-twist Mobius-aromatic conformation of [14]annulene. *Org Lett* **2005,** *7* (21), 4637.

129. Van-Catledge, F. A.; Allinger, N. L., Organic quantum chemistry. XXI. Structure and spectrum of cyclooctadecanonaene ([18]annulene). *J Am Chem Soc* **1969,** *91* (10), 2582.

130. Wannere, C. S.; Moran, D.; Allinger, N. L.; Hess, B. A., Jr.; Schaad, L. J.; Schleyer, P., On the stability of large [4n]annulenes. *Org Lett* **2003,** *5* (17), 2983.

131. Allinger, N. L.; Sprague, J. T., Conformational analysis. XC. Calculation of the structures of hydrocarbons containing delocalized electronic systems by the molecular mechanics method. *J Am Chem Soc* **1973,** *95* (12), 3893.

132. Kao, J.; Allinger, N. L., Conformational analysis. 122. Heats of formation of conjugated hydrocarbons by the force field method. *J Am Chem Soc* **1977,** *99* (4), 975.

133. King, R. A.; Crawford, T. D.; Stanton, J. F.; Schaefer, H. F., Conformations of [10]Annulene: More Bad News for Density Functional Theory and Second-Order Perturbation Theory. *J Am Chem Soc* **1999,** *121* (46), 10788.

134. Schleyer, P. V. R.; Maerker, C.; Dransfeld, A.; Jiao, H.; van Eikema Hommes, N. J. R., Nucleus-Independent Chemical Shifts: A Simple and Efficient Aromaticity Probe. *J Am Chem Soc* **1996,** *118* (26), 6317.

135. Schleyer, P. V.; Puhlhofer, F., Recommendations for the evaluation of aromatic stabilization energies. *Org Lett* **2002,** *4* (17), 2873.

136. Lungerich, D.; Nizovtsev, A. V.; Heinemann, F. W.; Hampel, F.; Meyer, K.; Majetich, G.; Schleyer, P. V.; Jux, N., [18]Annulene put into a new perspective. *Chem Comm* **2016,** *52* (25), 4710.

137. Price, D. R.; Stanton, J. F., Computational study of [10]annulene NMR spectra. *Org Lett* **2002,** *4* (17), 2809.

138. Bucher, G.; Grimme, S.; Huenerbein, R.; Auer, A. A.; Mucke, E.; Kohler, F.; Siegwarth, J.; Herges, R., Is the [9]annulene cation a Mobius annulene? *Angew Chem Int Ed* **2009,** *48* (52), 9971.

139. Mucke, E. K.; Kohler, F.; Herges, R., The [13]annulene cation is a stable Mobius annulene cation. *Org Lett* **2010,** *12* (8), 1708.

140. Baldridge, K. K.; Siegel, J. S., Ab Initio Density Funtional vs Hartree Fock Predictions for the Structure of[18]Annulene: Evidence for Bond Localization and Diminished Ring Currents in Bicycloannelated[18]Annulenes. *Angew Chem Int Ed* **1997,** *36* (7), 745.

141. Baumann, H., Importance of Electron Correlation in Computing Molecular Energies and Structures of Annulenes. *J Am Chem Soc* **1978,** *100* (23), 7196.

142. Thiel, W., Mndoc Study of Reactive Intermediates and Transition-States. *J Am Chem Soc* **1981,** *103* (6), 1420.

143. Dewar, M. J. S.; Haddon, R. C.; Student, P. J., Mindo/3 Study of [18]Annulene. *Chem Comm* **1974,** (14), 569.

144. Gorter, S.; Rutten-Keulemans, E.; Krever, M.; Romers, C.; Cruickshank, D. W. J., [18]-Annulene, C18H18, structure, disorder and Hückel's 4n + 2 rule. *Acta Crystallographica Section B Structural Science* **1995,** *51* (6), 1036.

145. Hirshfeld, F. L.; Rabinovich, D., The crystal structure of [18]annulene. II. Results. *Acta Crystallographica %@ 0365-110X* **1965,** *19* (2), 235.

146. Ermer, O., Concerning the structure of [18]annulene. *Helv Chim Acta* **2005,** *88* (8), 2262.

147. Sondheimer, F.; Wolovsky, R.; Amiel, Y., Unsaturated Macrocyclic Compounds. XXIII.1The Synthesis of the Fully Conjugated Macrocyclic Polyenes Cycloöctadecanonaene ([18]Annulene),2Cyclotetracosadodecaene ([24]Annulene), and Cyclotriacontapentadecaene ([30]Annulene). *J Am Chem Soc* **1962,** *84* (2), 274.

148. Heilbronner, E., Huckel Molecular Orbitals of Mobius-Type Conformations of Annulenes. *Tet Lett* **1964,** *5* (29-3), 1923.

149. Allen, W. D.; East, A. L. L.; Császár, A. G., In *Structures and Conformations of Non-Rigid Molecules*, Laane, J.; Dakkouri, M.; van der Veken, B.; Oberhammer, H., Eds. Kluwer: Dordrecht, 1993; pp 343.

150. Csaszar, A. G.; Allen, W. D.; Schaefer, H. F., In pursuit of the ab initio limit for conformational energy prototypes. *J Chem Phys* **1998,** *108* (23), 9751.

151. East, A. L. L.; Allen, W. D., The Heat of Formation of Nco. *J Chem Phys* **1993,** *99* (6), 4638.

152. Becke, A. D., Density-functional thermochemistry. III. The role of exact exchange. *J Chem Phys* **1993,** *98* (7), 5648.

153. Grimme, S., Semiempirical GGA-type density functional constructed with a long-range dispersion correction. *J Comput Chem* **2006,** *27* (15), 1787.

154. Becke, A., Density-Functional Thermochemistry. V. Systematic Optimization of Exchange-Correlation Functionals. *J Chem Phys* **1997,** *107*, 8554.

155. Zhao, Y.; Truhlar, D. G., The M06 suite of density functionals for main group thermochemistry, thermochemical kinetics, noncovalent interactions, excited states, and transition elements: two new functionals and systematic testing of four M06-class functionals and 12 other functionals. *Theo Chem Acc* **2008,** *120* (1-3), 215.

156. Becke, A. D., A new mixing of Hartree–Fock and local density-functional theories. *J Chem Phys* **1993,** *98* (2), 1372.

157. Lee, C.; Yang, W.; Parr, R. G., Development of the Colle-Salvetti correlation-energy formula into a functional of the electron density. *Phys Rev B Condens Matter* **1988,** *37* (2), 785.

158. Miehlich, B.; Savin, A.; Stoll, H.; Preuss, H., Results Obtained with the Correlation-Energy Density Functionals of Becke and Lee, Yang and Parr. *Chem Phys Lett* **1989,** *157* (3), 200.

159. Kang, J. K.; Musgrave, C. B., Prediction of transition state barriers and enthalpies of reaction by a new hybrid density-functional approximation. *J Chem Phys* **2001,** *115* (24), 11040.

160. Pinski, P.; Riplinger, C.; Valeev, E. F.; Neese, F., Sparse maps-A systematic infrastructure for reduced-scaling electronic structure methods. I. An efficient and simple linear scaling local MP2 method that uses an intermediate basis of pair natural orbitals. *J Chem Phys* **2015,** *143* (3), 034108.

161. Riplinger, C.; Sandhoefer, B.; Hansen, A.; Neese, F., Natural triple excitations in local coupled cluster calculations with pair natural orbitals. *J Chem Phys* **2013,** *139* (13), 134101.

162. Riplinger, C.; Neese, F., An efficient and near linear scaling pair natural orbital based local coupled cluster method. *J Chem Phys* **2013,** *138* (3), 034106.

163. Neese, F.; Hansen, A.; Liakos, D. G., Efficient and accurate approximations to the local coupled cluster singles doubles method using a truncated pair natural orbital basis. *J Chem Phys* **2009,** *131* (6), 064103.

164. Neese, F., Software update: the ORCA program system, version 4.0. *Wiley Interdiscip Rev Comput Mol Sci* **2018,** *8* (1).

165. Ruscic, B.; Pinzon, R. E.; Morton, M. L.; von Laszevski, G.; Bittner, S. J.; Nijsure, S. G.; Amin, K. A.; Minkoff, M.; Wagner, A. F., Introduction to Active Thermochemical Tables: Several “Key” Enthalpies of Formation Revisited†. *J Phys Chem A* **2004,** *108* (45), 9979.

166. Kruszewski, J.; Krygowski, T. M., Definition of aromaticity basing on the harmonic oscillator model. *Tet Lett* **1972,** *13* (36), 3839.

167. Krygowski, T. M., Crystallographic studies of inter- and intramolecular interactions reflected in aromatic character of .pi.-electron systems. *J Chem Info Model* **1993,** *33* (1), 70.

168. Simon, L.; Paton, R. S., The True Catalyst Revealed: The Intervention of Chiral Ca and Mg Phosphates in Bronsted Acid Promoted Asymmetric Mannich Reactions. *J Am Chem Soc* **2018,** *140* (16), 5412.

169. Formica, M.; Sorin, G.; Farley, A. J. M.; Diaz, J.; Paton, R. S.; Dixon, D. J., Bifunctional iminophosphorane catalysed enantioselective sulfa-Michael addition of alkyl thiols to alkenyl benzimidazoles. *Chem Sci* **2018,** *9* (34), 6969.

170. Paton, R. S.; Goodman, J. M.; Pellegrinet, S. C., Mechanistic insights into the catalytic asymmetric allylboration of ketones: Bronsted or Lewis acid activation? *Org Lett* **2009,** *11* (1), 37.

171. Simon, L.; Paton, R. S., QM/MM study on the enantioselectivity of spiroacetalization catalysed by an imidodiphosphoric acid catalyst: how confinement works. *Org Biomol Chem* **2016,** *14* (11), 3031.

172. Yamanaka, T.; Kondoh, A.; Terada, M., Kinetic resolution of racemic amino alcohols through intermolecular acetalization catalyzed by a chiral Bronsted acid. *J Am Chem Soc* **2015,** *137* (3), 1048.

173. Christ, P.; Lindsay, A. G.; Vormittag, S. S.; Neudorfl, J. M.; Berkessel, A.; O'Donoghue, A. C., pKa values of chiral Bronsted acid catalysts: phosphoric acids/amides, sulfonyl/sulfuryl imides, and perfluorinated TADDOLs (TEFDDOLs). *Chemistry* **2011,** *17* (31), 8524.

174. Milo, A.; Bess, E. N.; Sigman, M. S., Interrogating selectivity in catalysis using molecular vibrations. *Nature* **2014,** *507* (7491), 210.

175. Milo, A.; Neel, A. J.; Toste, F. D.; Sigman, M. S., Organic chemistry. A data-intensive approach to mechanistic elucidation applied to chiral anion catalysis. *Science* **2015,** *347* (6223), 737.

176. Changotra, A.; Sunoj, R. B., Origin of Kinetic Resolution of Hydroxy Esters through Catalytic Enantioselective Lactonization by Chiral Phosphoric Acids. *Org Lett* **2016,** *18* (15), 3730.

177. Jindal, G.; Sunoj, R. B., Axially chiral imidodiphosphoric Acid catalyst for asymmetric sulfoxidation reaction: insights on asymmetric induction. *Angew Chem Int Ed* **2014,** *53* (17), 4432.

178. Malakar, S.; Shree Sowndarya, S. V.; Sunoj, R. B., A quantification scheme for non-covalent interactions in the enantio-controlling transition states in asymmetric catalysis. *Org Biomol Chem* **2018,** *16* (31), 5643.

179. Nimmagadda, S. K.; Mallojjala, S. C.; Woztas, L.; Wheeler, S. E.; Antilla, J. C., Enantioselective Synthesis of Chiral Oxime Ethers: Desymmetrization and Dynamic Kinetic Resolution of Substituted Cyclohexanones. *Angew Chem Int Ed* **2017,** *56* (9), 2454.

180. Falcone, B. N.; Grayson, M. N.; Rodriguez, J. B., Mechanistic Insights into a Chiral Phosphoric Acid-Catalyzed Asymmetric Pinacol Rearrangement. *J Org Chem* **2018,** *83* (23), 14683.

181. Grayson, M. N.; Yang, Z.; Houk, K. N., Chronology of CH...O Hydrogen Bonding from Molecular Dynamics Studies of the Phosphoric Acid-Catalyzed Allylboration of Benzaldehyde. *J Am Chem Soc* **2017,** *139* (23), 7717.

182. Rodríguez, E.; Grayson, M. N.; Asensio, A.; Barrio, P.; Houk, K. N.; Fustero, S., Chiral Brønsted Acid-Catalyzed Asymmetric Allyl(propargyl)boration Reaction of ortho-Alkynyl Benzaldehydes: Synthetic Applications and Factors Governing the Enantioselectivity. *ACS Catal* **2016,** *6* (4), 2506.

183. Ingle, G. K.; Liang, Y.; Mormino, M. G.; Li, G.; Fronczek, F. R.; Antilla, J. C., Chiral magnesium BINOL phosphate-catalyzed phosphination of imines: access to enantioenriched alpha-amino phosphine oxides. *Org Lett* **2011,** *13* (8), 2054.

184. Larson, S. E.; Li, G.; Rowland, G. B.; Junge, D.; Huang, R.; Woodcock, H. L.; Antilla, J. C., Catalytic asymmetric aza-Darzens reaction with a vaulted biphenanthrol magnesium phosphate salt. *Org Lett* **2011,** *13* (9), 2188.

185. Zhang, Z.; Zheng, W.; Antilla, J. C., Highly enantioselective catalytic benzoyloxylation of 3-aryloxindoles using chiral VAPOL calcium phosphate. *Angew Chem Int Ed* **2011,** *50* (5), 1135.

186. Zheng, W.; Zhang, Z.; Kaplan, M. J.; Antilla, J. C., Chiral calcium VAPOL phosphate mediated asymmetric chlorination and Michael reactions of 3-substituted oxindoles. *J Am Chem Soc* **2011,** *133* (10), 3339.

187. Nakamura, S.; Ohara, M.; Koyari, M.; Hayashi, M.; Hyodo, K.; Nabisaheb, N. R.; Funahashi, Y., Desymmetrization of meso-aziridines with TMSNCS using metal salts of novel chiral imidazoline-phosphoric acid catalysts. *Org Lett* **2014,** *16* (17), 4452.

188. Della Sala, G., Studies on the true catalyst in the phosphate-promoted desymmetrization of meso-aziridines with silylated nucleophiles. *Tetrahedron* **2013,** *69* (1), 50.

189. Wang, Z.; Law, W. K.; Sun, J., Chiral phosphoric acid catalyzed enantioselective desymmetrization of meso-epoxides by thiols. *Org Lett* **2013,** *15* (23), 5964.

190. Ajitha, M. J.; Huang, K. W., Role of keto-enol tautomerization in a chiral phosphoric acid catalyzed asymmetric thiocarboxylysis of meso-epoxide: a DFT study. *Org Biomol Chem* **2015,** *13* (45), 10981.

191. Grimme, S.; Antony, J.; Ehrlich, S.; Krieg, H., A consistent and accurate ab initio parametrization of density functional dispersion correction (DFT-D) for the 94 elements H-Pu. *J Chem Phys* **2010,** *132* (15), 154104.

192. Grimme, S., Semiempirical GGA-Type Density Functional Constructed with a Long-Range Dispersion Correction. *J. Comp. Chem.* **2006,** *27*, 1787.

193. Tomasi, J.; Mennucci, B.; Cammi, R., Quantum mechanical continuum solvation models. *Chem. Rev.* **2005,** *105* (8), 2999.

194. Grimme, S., Supramolecular Binding Thermodynamics by Dispersion-Corrected Density Functional Theory. *Chem. Eur. J.* **2012,** *18* (32), 9955.

195. These quasi-RRHO free energy differences are in much better agreement with the experimental er values than those derived from the standard RRHO approximation.

196. Grimme, S.; Antony, J.; Ehrlich, S.; Krieg, H., A Consistent and Accurate *ab Initio* Parametrization of Density Functional Dispersion Correction (DFT-D) for the 94 Elements H-Pu. *J Chem Phys* **2010,** *132*, 154104.

197. Crabtree, R. H.; Lei, A., Introduction: CH Activation. *Chem Rev* **2017,** *117* (13), 8481.

198. Ackermann, L.; Vicente, R.; Kapdi, A. R., Transition-metal-catalyzed direct arylation of (hetero)arenes by C-H bond cleavage. *Angew Chem Int Ed* **2009,** *48* (52), 9792.

199. Chen, X.; Engle, K. M.; Wang, D. H.; Yu, J. Q., Palladium(II)-catalyzed C-H activation/C-C cross-coupling reactions: versatility and practicality. *Angew Chem Int Ed* **2009,** *48* (28), 5094.

200. Ackermann, L., Carboxylate-assisted ruthenium-catalyzed alkyne annulations by C-H/Het-H bond functionalizations. *Acc Chem Res* **2014,** *47* (2), 281.

201. Jin, Z.; Chu, L.; Chen, Y. Q.; Yu, J. Q., Pd-Catalyzed Remote Meta-C-H Functionalization of Phenylacetic Acids Using a Pyridine Template. *Org Lett* **2018,** *20* (2), 425.

202. Chu, L.; Shang, M.; Tanaka, K.; Chen, Q.; Pissarnitski, N.; Streckfuss, E.; Yu, J. Q., Remote Meta-C-H Activation Using a Pyridine-Based Template: Achieving Site-Selectivity via the Recognition of Distance and Geometry. *ACS Cent Sci* **2015,** *1* (7), 394.

203. Bag, S.; Jayarajan, R.; Mondal, R.; Maiti, D., Template-Assisted meta-C-H Alkylation and Alkenylation of Arenes. *Angew Chem Int Ed* **2017,** *56* (12), 3182.

204. Dutta, U.; Modak, A.; Bhaskararao, B.; Bera, M.; Bag, S.; Mondal, A.; Lupton, D. W.; Sunoj, R. B.; Maiti, D., Catalytic Arene meta-C–H Functionalization Exploiting a Quinoline-Based Template. *ACS Catal* **2017,** *7* (5), 3162.

205. Bay, K. L.; Yang, Y.-F.; Houk, K. N., Multiple roles of silver salts in palladium-catalyzed C–H activations. *J Organomet Chem* **2018,** *864*, 19.

206. Masui, K.; Ikegami, H.; Mori, A., Palladium-catalyzed C-H homocoupling of thiophenes: facile construction of bithiophene structure. *J Am Chem Soc* **2004,** *126* (16), 5074.

207. Neo, Y. C.; Vittal, J. J.; Andy Hor, T. S., Pd(O2CCF2CF3-O)2(dppf) and PdAg(μ-O2CCF2CF3)2(O2CCF2CF3-O)(dppf) [dppf = 1,1′-bis(diphenylphosphino)ferrocene]: A stable Pd(ii) phosphine carboxylate as a precursor to heterobimetallic carboxylates. *Dalton Trans* **2002,** (3), 337.

208. Anand, M.; Sunoj, R. B.; Schaefer, H. F., Palladium–Silver Cooperativity in an Aryl Amination Reaction through C–H Functionalization. *ACS Catal* **2015,** *6* (2), 696.

209. Achar, T. K.; Zhang, X.; Mondal, R.; Shanavas, M. S.; Maiti, S.; Maity, S.; Pal, N.; Paton, R. S.; Maiti, D., Palladium-Catalyzed Directed meta-Selective C-H Allylation of Arenes: Unactivated Internal Olefins as Allyl Surrogates. *Angew Chem Int Ed* **2019,** *58* (30), 10353.

210. Schafer, A.; Horn, H.; Ahlrichs, R., Fully Optimized Contracted Gaussian-Basis Sets for Atoms Li to Kr. *J Chem Phys* **1992,** *97* (4), 2571.

APPENDIX A

SUPPLEMENTARY INFORMATION RELATED TO COMPUTATIONAL STUDIES OF AZA-THIA CRYPTANDS

Free energy surfaces for the rotameric interconversion of L7 and for the *in/out* topomeric interconversion of L8.

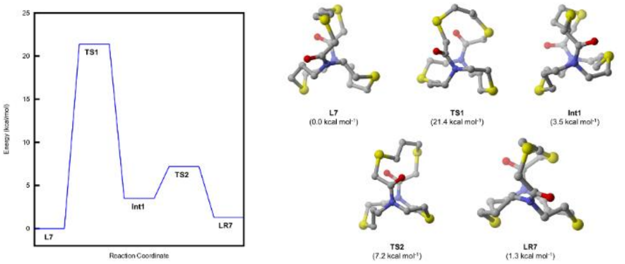

Figure 18 Interconversion of L7 between its two rotameric forms computed at the ωB97X-D/def2tzvp/b97d/def2tzvp in kcal/mol.

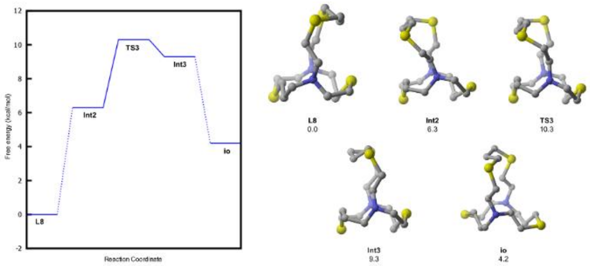

Figure 19 Topomeric interconversion of L8 (in/in topomer) to L8 (in/out topomer) computed at the ωB97X-D/def2tzvp/b97d/def2tzvp in kcal/mol.

APPENDIX B

SUPPLEMENTARY INFORMATION RELATED TO [18]ANNULENE: A MORE COMPLETE STORY

Table 11 ZPVE corrected DFT energies with 6-311+G(d,p) basis set

Conformer	B3LYP	BHandHLYP	KMLYP	B97D	M06-2X	ωB97X-D
1	0.0	0.9	1.4	0.0	1.1	2.8
2	0.0	0.0	0.0	0.0	0.0	0.0
3	5.3	4.0	3.7	5.3	3.0	2.8
4	6.4	3.9	3.3	5.7	2.0	1.9
5	8.3	5.4	4.7	7.3	3.4	10.0
6	9.7	8.4	8.3	9.8	7.6	7.2
7	6.1	3.8	3.2	5.1	1.9	1.7
8	7.1	4.5	3.7	6.1	2.2	1.7
9	7.5	5.5	5.1	6.8	3.9	3.5
17	11.4	4.5	3.7	6.1	2.2	9.0

Table 12 ZPVE corrected DFT energies with def2-TZVP basis set

Conformer	B3LYP	BHandHLYP	KMLYP	B97D	M06-2X	ωB97X-D
1	0.0	0.0	0.4	0.0	0.6	2.8
2	1.0	0.1	0.0	0.5	0.0	0.0
3	6.3	4.3	4.0	6.1	3.4	3.3
4	7.6	4.3	3.8	6.6	2.6	2.6
5	9.6	5.9	5.3	8.3	4.0	3.6

6	10.8	8.7	8.6	10.5	8.0	7.7
7	7.4	4.2	3.6	6.1	2.4	2.4
8	8.3	5.0	4.3	7.0	2.8	2.5
9	8.8	6.0	5.6	7.8	4.5	4.2
17	12.4	13.3	10.7	12.0	10.0	9.3

Table 13 DLPNO-CCSD(T)/cc-pVTZ electronic energies for geometries optimized at DFT methods with def2-TZVP basis set

Conformer	B3LYP	BHandHLYP	KMLYP	B97D	M06-2X	ωB97X-D
1	0.0	1.2	1.1	0.0	1.5	1.6
2	0.0	0.0	0.0	0.3	0.0	0.0
3	6.1	2.8	2.8	6.1	2.8	2.8
4	7.5	2.4	2.4	5.5	2.4	2.4
5	8.3	3.4	3.4	9.6	3.4	3.4
6	11.7	7.1	7.2	11.6	7.2	7.2
7	5.8	2.3	2.3	5.7	2.4	2.4
8	6.5	2.3	2.3	6.4	2.4	2.4
9	7.5	3.9	3.9	7.3	4.1	4.0
17	12.2	13.5	9.3	10.3	9.3	9.4

Table 14 Incremental focal point table for computing DLPNO-CCSD(T) electronic energy difference of **1** with respect to **2** at the complete basis set limit for geometries optimized at ΩB97X-D/def2-TZVP level of theory

	HF	**+δSLMP2**	**+δDLPNO-CCSD**	**+δDLPNO-CCSD(T)**	**= DLPNO-CCSD(T)**
cc-pVDZ	+23.14	-45.83	+32.60	-7.79	+2.12
cc-pVTZ	+23.01	-42.79	+29.25	-7.84	+1.63
cc-pVQZ	+23.17	-42.72	+28.72	-7.80	+1.38
cc-pV5Z	+23.11	-42.67	[+28.72]	[-7.80]	[+1.36]
CBSLIMIT	[+23.05]	[-42.61]	[+28.72]	[-7.80]	[+1.36]

Table 15 DLPNO-CCSD(T)/cc-pVTZ//ωB97X-D/def2-TZVP enthalpies for transition states for inner/outer proton interconversion in [18]annulene conformers (TS connecting conformers X, Y=T_{XY}) in kcal/mol.

Structure	ΔH_{QRRHO}
2	0.0
TS_{23}	12.4
TS_{34}	12.1
TS_{36}	16.1
TS_{38}	11.5
TS_{45}	12.9
TS_{417}	12.4
TS_{49}	14.7
TS_{47}	12.4
TS_{617}	19.1
TS_{67}	14.5
TS_{69}	15.1
TS_{89}	12.2
TS_{87}	13.8

APPENDIX C

SUPPLEMENTARY INFORMATION RELATED TO ROLE OF ALKALI METALS IN CHIRAL PHOSPHORIC ACID CATALYSIS

Table 16 Computed quasi-RRHO free energies at the ωB97X-D/def2-TZVP//B97-D/def2-TZVP level of theory for all the conformers relative to the major enantiomer for the reaction R2 (M=Li) in Table 8 in kcal/mol.

TS Structure	ΔG_{QRRHO}	TS Structure	ΔG_{QRRHO}
TS11_SS	0.0	TS6_RR	2.5
TS17_SS	0.5	TS1_RR	2.6
TS18_SS	0.9	TS20_SS	2.6
TS15_SS	1.0	TS22_SS	2.7
TS13_SS	1.4	TS8_RR	3.1
TS12_SS	1.7	TS7_RR	3.1
TS4_RR	1.8	TS23_SS	4.1
TS21_SS	2.4	TS16_SS	4.6
TS2_RR	2.4	TS24_SS	4.8
TS19_SS	2.5	TS10_RR	6.4

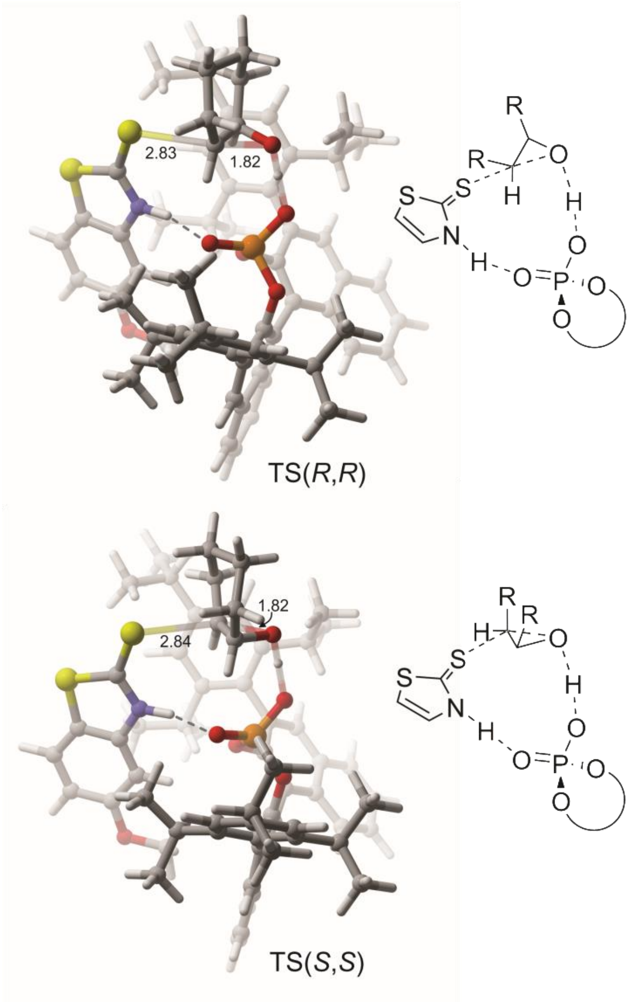

Figure 20 Lowest-lying TS geometries for CPA-catalyzed epoxide desymmetrization reaction R1 in Table 8 reported by Seguin *et al*.[49] [Figure adapted with permission of the journal, *ACS Catalysis*, **2016**, 6, 2681-2688]

Table 17 Electrostatic interaction energy for TS leading to the minor enantiomer (*R*,*R*) for the reaction R2 (M=Li) in Table 8 with SH…O distance of 1.64 A relative to the major enantiomer (*S*,*S*). (Energies in kcal/mol)

TS	$\Delta\Delta E$	$\Delta\Delta E_{\text{Electrostatic}}$
TS6_RR	2.8	3.6

APPENDIX D

SUPPLEMENTARY INFORMATION RELATED TO MECHANISTIC STUDIES INVESTIGATING THE ROLE OF HEXAFLUOROISOPROPANOL AND ADDITIVES IN META C-H FUNCTIONALIZATION OF ARENES

Table 18 Computed enthalpy barriers for C-H activation with zero, one and two explicit HFIP molecules at ωB97X-D/def2-TZVP//B97-D/def2-SVP level of theory in kcal/mol.

#HFIP	**0**			**1**			**2**		
Active Catalyst	**ortho**	**meta**	**para**	**ortho**	**meta**	**para**	**ortho**	**meta**	**para**
Cat_A	36.1	48.1	39.9	31.1	44.9	31.0	26.7	36.9	27.9
Cat_B	30.4	31.1	30.7	27.7	28.6	28.1	23.0	22.7	23.6
Cat_C	31.2	30.8	29.5	28.6	27.7	27.1	24.6	24.3	23.9
Cat_D	28.3	28.9	28.1	25.7	25.1	26.0	23.8	25.4	23.3
Cat_E	30.2	31.1	29.1	28.1	27.4	25.4	23.2	22.1	21.6
Cat_F	29.9	29.4	30.1	26.7	26.9	26.4	24.1	23.2	22.3

Table 19 Computed enthalpy barriers for 1,2-migratory insertion with zero, one and two explicit HFIP molecules at ωB97X-D/def2-TZVP//B97-D/def2-SVP level of theory in kcal/mol.

#HFIP	**0**			**1**			**2**		
Active Catalyst	**ortho**	**meta**	**para**	**ortho**	**meta**	**para**	**ortho**	**meta**	**para**
Cat_A	33.3	29.8	35.5	31.6	27.4	31.9	30.0	23.5	29.2
Cat_B	37.1	32.7	32.1	32.4	28.6	30.4	32.1	24.7	28.0
Cat_C	35.8	32.5	31.6	33.9	30.3	29.8	31.2	27.3	28.6
Cat_D	36.2	33.8	31.1	32.1	30.7	29.4	31.7	27.4	27.2
Cat_E	34.2	33.2	33.8	31.0	29.4	31.1	30.4	26.5	26.9
Cat_F	34.6	33.7	34.0	31.5	31.8	30.2	32.1	26.8	27.5